Composites: Part A 177 (2024) 107936

Contents lists available at ScienceDirect

Composites Part A

journal homepage: www.elsevier.com/locate/compositesa

A comprehensive experimental and modeling study of the strain rate- and temperature-dependent deformation behavior of bio-degradable Mg-CeO_2 nanocomposites

Surja Deka [a], Farzin Mozafari [b], Ashis Mallick [a,*]

[a] Department of Mechanical Engineering, Indian Institute of Technology (ISM) Dhanbad, Jharkhand, India
[b] Department of Mechanical Engineering, Abdullah Gül University, Kayseri, Turkey

ARTICLE INFO

Keywords:
B. high-temperature properties
B. mechanical properties
D. microstructural analysis
Machine learning

ABSTRACT

A comprehensive study was undertaken on the temperature-dependent and strain rate-sensitive deformation behavior of near-dense low-volume fraction magnesium-cerium dioxide (Mg-CeO_2) nanocomposites synthesized by powder metallurgy technique. The process involved ball milling of elemental powders → cold compaction → sintering in an inert atmosphere, and in-situ hot extrusion. The Mg-CeO_2 nanocomposites displayed strain rate and temperature sensitivity, exhibiting higher yield strength, superior compressive characteristics, greater hardness, and improved ductility compared to pure Mg and most commercial Mg alloys. Furthermore, a thorough micro-structural investigation was conducted to characterize the distributions of ceria nanoparticles, grain refinement degree, ceria-magnesium interface, formation of deformation twins and interfacial bonding between the reinforcement and matrix. The present study has proposed two modeling approaches, the Johnson–Cook (J–C) constitutive model and a machine learning-assisted model, to predict the mechanical behavior of monolithic Mg and Mg-CeO_2 nanocomposites. The models effectively explained the deformation behavior under various strain rates and temperatures.

1. Introduction

Over the years, researchers have been engaged in developing lightweight materials with superior physical and mechanical characteristics to meet the increasingly stringent weight and efficiency requirements for components in various areas of engineering, such as automotive, aerospace, and structural fields [1–3]. In other words, materials having high specific strength, low density, high toughness, high damping potential, ease of recovery and recycling, magnesium alloy and nanocomposites, etc., are being increasingly used in the aerospace, electronics, and automotive industries to improve energy efficiency, maximize component safety factors, and enhance equipment performance [4,5].

In recent years, the demand for bio-degradable materials having modulus properties similar to those of human bones has been growing rapidly. As a result, Mg-based materials have become promising alternatives for biomedical applications [6]. However, due to their low strength, low hardness, poor ductility, weak creep resistance, low corrosion resistance, and susceptibility to easy ignition, Mg-based materials have a narrow range of applications as structural components and in biomedical applications [7]. To date, several methods have been explored to improve the characteristics of Mg-based materials for use in structural and biological applications.

In recent years, the incorporation of the NPs to strengthen the Mg-based materials has generated substantial scientific interest due to the high commercial prospects of developing innovative composites with superior mechanical characteristics [1,8]. The literature review reveals that a number of investigations have been conducted which added various nano-scale reinforcements, such as TiB_2, SiC, TiC, Al_2O_3, and CNT, to the Mg-based matrix so as to concurrently boost strength and ductility [4]. Among various types of ceramic oxide NPs, rare-earth oxide (REO) NPs have shown to be the most effective in reducing the segregation of the grain boundaries and in refining the microstructure of the materials [9]. REOs can be used in dispersion strengthening phase because of their strong resistance to coarsening of the microstructure, which is essential for producing improved multifunctional metallic matrix composites with high strength and ductility [1]. Furthermore, as REOs are thermally stable reinforcements, they can be used at exceedingly high temperature [10]. A recent research by Kujur et al. [11] examined the ignition, compression and damping properties of Mg-Sm_2O_3 nanocomposites. The study found that their

* Corresponding author.
E-mail address: mal123_us@yahoo.com (A. Mallick).

https://doi.org/10.1016/j.compositesa.2023.107936
Received 22 June 2023; Received in revised form 1 November 2023; Accepted 26 November 2023
Available online 28 November 2023
1359-835X/

ignition temperature was at least 650 °C, which is higher than the ignition temperature of most of the Mg alloys, such as ZK40 A, AZ61, AM50, ZK60 A, and AZ91 A. These nanocomposites are used in commercial aircraft as well as in alloys like WE43T, which are approved by Federal Aviation Administration. Moreover, the study reported a marked increase in hardness and compressive strength of Mg-Sm_2O_3 nanocomposites by ~37% and ~53%, respectively, over the monolithic Mg. Haghshenas et al. [9] explored the nano indentation-driven response of Mg-Sm_2O_3 nanocomposites wherein they reported a substantial increase in the hardness and elastic modulus properties. These noticeable improvements in the REO-reinforced Mg nanocomposites proved to be a strong impetus for developing novel REO-containing Mg-based composites with improved material characteristics.

As an REO with superior material characteristics, CeO_2 demonstrates improved mechanical behavior in metal matrix nanocomposites (MMNC) [6,12]. Furthermore, CeO_2 has been utilized in various electro deposited MMNCs due to its corrosion resistant properties [13]. In addition, it offers greater hardness and wear resistance [14]. Furthermore, CeO_2 has biomedical applications, particularly in nanobiology, because of its high regeneration qualities as a result of its low reduction potential [12].

There have only been a few instances when CeO_2 NPs were added to the Mg MMNC to study their characteristics. Recently, Kujur et al. [12] examined the influence of CeO_2 NPs on Mg's mechanical, damping, and ignition characteristics. The study reported a significant enhancement in the compressive strength and fracture strain values of the magnesium-cerium dioxide (Mg-CeO_2) nanocomposites. Mg-1.5CeO_2 displayed the maximum ultimate compressive strength (UCS) of 329 MPa, which was 32% higher than that of the monolithic Mg. Moreover, the Mg-1.0CeO_2 nanocomposites showed the maximum compressive fracture strain (CFS) value of 25.8%, which was 48% higher than that of pure Mg. Despite exhibiting higher compressive strength values, it cannot be used for applications such as in the biomedical field, wherein in cases, the implant material calls for an initial compressive strength of at least 400 MPa [15]. Therefore, this research will serve as a base for future studies, and further investigation and experimentation into improving the material properties is strongly recommended in order to be relevant with regard to the automotive and structural industries, which require materials with high stiffness, modulus, and strength values. In another study, Kujur and his team examined the CeO_2-reinforced Mg-Zn nanocomposites from a mechanical and biological standpoint, demonstrating favorable mechanical properties and corrosion resistance [6]. However, as previously noted, the strength of the nanocomposites could be improved, and greater emphasis should be placed on high-temperature testing, as Mg-based nanocomposites are used in high-temperature engineering applications [16]. Furthermore, neither of the studies discussed the strain rate-dependent behavior of Mg-CeO_2 and Mg-Zn/CeO_2 nanocomposites, which should be rigorously explored because Mg-based nanocomposites are highly dependent on the strain rate due to their densely packed and hexagonal crystallographic structures [17].

The accurate prediction of mechanical properties is crucial for the use of innovative nanocomposites in engineering design. Various models, including molecular dynamics (MD) simulation, micro-mechanical modeling, phenomenological, physically-based, and artificial neural network (ANN) models, are employed to determine the mechanical behavior of these materials [18–24]. Zhang et al. [18] used MD simulation to predict Young's modulus of a graphene-reinforced copper (Gr/Cu) nanocomposite but obtained a value (157.26 GPa) higher than the experimental result (97 GPa). This discrepancy may arise from the different reinforcement arrangements in simulations and experiments. Laksmi et al. [19] utilized micro-mechanics modeling to predict Young's modulus of a 5 wt.%-Al composite, yielding a higher value (130 GPa) compared to the experimental result (88 GPa) due to the assumption of perfect bonding at the reinforcement-matrix interface. The Johnson–Cook (J–C) model, with its simple multiplication-based approach, was effectively employed in finite element analysis to represent the flow behavior of materials at elevated temperatures, as demonstrated by Zhang et al. [21] in their examination of AZ31 alloy's uni-axial compression behavior. While conventional theoretical models present computational challenges, machine learning (ML) techniques have emerged as a promising solution for determining correlations between the complex materials' position and engineering qualities. Rahmani et al. [25] successfully used an ANN model to evaluate the tensile properties of TiO_2- and ZrO_2-based Mg nanocomposites, while Najjar et al. [23] applied an ML algorithm to estimate the yield and tangent stresses of Cu-Al2O3 nanocomposites. Therefore, these studies show that Ml-based approaches can potentially offer a powerful tool for modeling complex materials with disordered microstructures such as nanocomposites, and supporting their design and engineering applications.

The findings from the literature review show that no studies have so far been made on the synthesis of Mg-CeO_2 nanocomposites by employing high-energy ball milling and in-situ hot extrusion-assisted PM processes. The present study investigated how high-energy ball milling and reinforcement content influence the mechanical and microstructural properties of the monolithic Mg and Mg-CeO_2 nanocomposites. Further, an investigation into the high-temperature compression capabilities of the nanocomposites was also attempted to find out their applications at high temperatures. The findings from the literature also revealed that no research has been conducted to discuss the rate-sensitive behavior of the Mg-CeO_2 nanocomposites. The present authors, therefore, specially monitored the rate-sensitive compression behavior at room temperature and at raised temperatures. Finally, two distinct modeling approaches were examined during this investigation to describe the strain rate- and temperature-dependent flow behavior of the monolithic Mg and Mg-CeO_2 nanocomposites. First, the J–C constitutive theory was employed due to its highly predictive capabilities regarding the hot deformation behavior of composites having complex microstructures at various strain rates and temperatures. Secondly, an ML-assisted setting was developed, based on a multilayer perceptron (MLP) network with a back-propagation learning algorithm. A data preparation strategy, including an ad-hoc data normalization algorithm, was proposed to train the proposed network efficiently and verify it rigorously by using the experiment data sets. The diverse sets of strain rate- and temperature-dependent flow behavior, reproduced by the J–C constitutive model and the MLP network with a back-propagation learning algorithm were verified by comparing them with the experiment data.

2. Experimental methodology

2.1. Materials and synthesis

The present study used high purity (≥ 99%) Mg powder with a particle size of 32 μm as the matrix material, which was procured from Sigma Aldrich (USA). The reinforcing agent used to prepare the nanocomposites was CeO_2 (purity ≥ 99.5%) with an average particle size of 50 nm, purchased from Alfa Aesar Corporation (Ward Hill, MA, USA).

2.2. Preparation of the nanocomposites

The Mg-based MMNCs were fabricated using a PM process (please refer to the schematic figure, Fig. 1(a)). The proposed synthesizing process involved ball milling of the powder mixture (Mg powder and CeO_2 NPs) in an attributor mill. The parameters used in the milling process are ball-to-powder ratio = 10:1, the rotation speed of vial = 250 rpm and ball size = 16 mm. The volume percentage (vol.%) of the reinforcements taken were 0.5, 1.0, and 1.5, respectively, which was decided on the basis of the previous work by the present authors [6]. The primary reason for the ball milling of powder mixtures was to

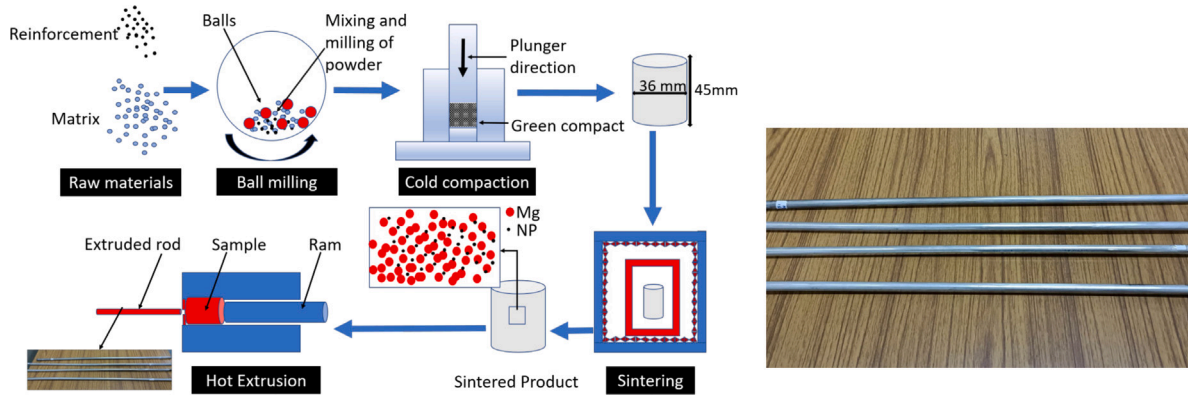

Fig. 1. (a) Flowchart of the synthesis procedure, and (b) final extruded rods of pure Mg and Mg-CeO_2 nanocomposites. From the bottom to the top, the sequence of the rods is pure Mg, Mg-0.5CeO_2, Mg-1.0CeO_2 and Mg-1.5CeO_2. No evidence of surface crack can be seen in all the extruded rods.

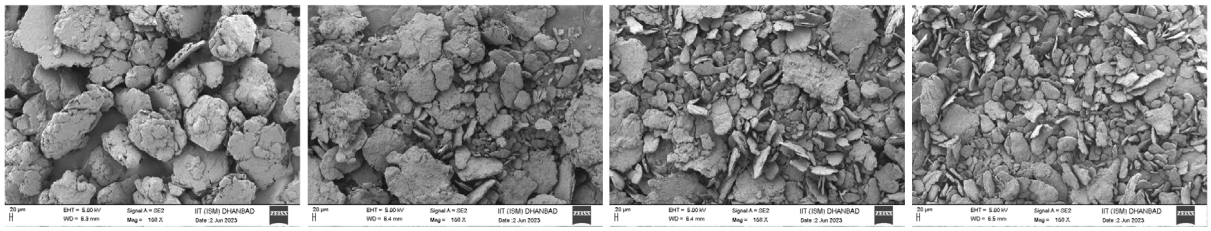

Fig. 2. Representative FESEM micrographs of powders milled for 5 hours: (a) Pure Mg, (b) Mg-0.5CeO_2, (c) Mg-1.0CeO_2, and (d) Mg-1.5CeO_2 nanocomposites.

homogeneously disperse CeO_2 NPs in the Mg matrix and refine the particulate size. Zinc stearate was added as a process control agent (1.5 wt.%) to avoid cold welding and agglomeration of powder particles during the milling process. Next, cold compaction of the homogeneously mixed powder was carried out in a cylindrical die (36 mm diameter and 80 mm height) by imposing a 50-tonne load to make the green compacts (35 mm in diameter and 45 mm in length). After successful consolidation, the green compacts were sintered at a temperature of 500 °C (~77% of the melting temperature of Mg) in a tubular furnace in an argon atmosphere. Finally, hot extrusion was carried out in the argon atmosphere at 400 °C with an extrusion ratio of 20.25:1.

2.3. Characterization methods

Microstructural characterization of the nanocomposite samples has been done with the help of optical microscopy (OM, Model: DMI Optima, Dewinter Optical Inc, India), field emission scanning electron microscopy (FESEM, Supra 55, Zeiss, Germany) with energy dispersive spectroscopy (EDS), and X-ray diffraction (XRD, Rigaku, USA). For OM, the samples were grinded and polished and then chemically etched in an acetic-picral solution (4.2 gm of picric acid, 70 ml ethanol, 10 ml acetic acid, and 10 ml distilled water) for 20 s to determine their microstructural features (grain boundaries, corresponding grain structure, phases, and micropores). Further observations were made using XRD analysis equipped with Cu-Kα radiation (wavelength of 0.154 nm) at a scan rate of 4°/min over a scanning range from 20 to 80°. The crystallite size of the nanocomposite powder samples were measured from the XRD data by utilizing the William–Hall (W–H) equation [26].

In order to make sure that the synthesizing process yielded samples with proper densification, a densification study was conducted using Archimedes' principle. It is important to iterate that the PM products exhibit inevitable porosity. Hence, a porosity analysis was undertaken using the rule of mixture [27]. It helped understand the wettability characteristics, particle agglomeration, clustering, and nucleation at the interface of the NPs and the matrix.

The American Society for Testing and Materials (ASTM) regulations were followed in preparing the samples for microhardness and compression (ASTM E9) tests. Hardness tests were conducted on the polished samples by using a Vickers hardness testing machine (Model: MTR3/50-50/NI instrument, MICROTEST S.A., Spain). It maintained a loading rate and dwell time of 5 N/min and 30 s, respectively. The tests were repeated eight times to ensure uniformity in the readings. Next, the compressive tests were performed on test specimens characterized by a length-to-diameter ratio of 1:1. The physical dimensions of the samples were measured to be 8 mm in length and diameter. ASTM-E9-89a was followed in preparing the samples which allow an aspect ratio range of 0.8 to 10.0 for metallic materials. In order to eliminate any residual grease and oil, the end of the samples and fixture-bearing blocks were thoroughly cleansed using acetone. Then, the samples were placed in the test fixture and carefully aligned with the fixture to ensure concentric loading. Teflon sheets were employed as an intermediary layer between the specimens and platens in order to minimize friction. The machine's crosshead speeds were adjusted to 4.8 mm/min, 0.48 mm/min, and 0.048 mm/min, which corresponded to strain rates of 0.01 s^{-1}, 0.001 s^{-1}, and 0.0001 s^{-1}, respectively. High-temperature compression experiments were performed using an INSTRON-8801 machine that has a sealed chamber at temperatures of 100, 150 and 200 °C. An inbuilt heater efficiently provided the necessary heat for this chamber, and a temperature control unit with excellent accuracy (±1 °C) allowed for temperature regulation. For every test, the samples were soaked for 20 min after reaching the specified temperatures so that a temperature equilibrium could be attained within the samples. The compression tests were repeated three times to ensure consistency in the measurements. Following the compression tests, a fractography analysis of the Mg-CeO_2 samples was done to understand the different fracture mechanisms that the nanocomposites underwent at room temperature and elevated temperatures.

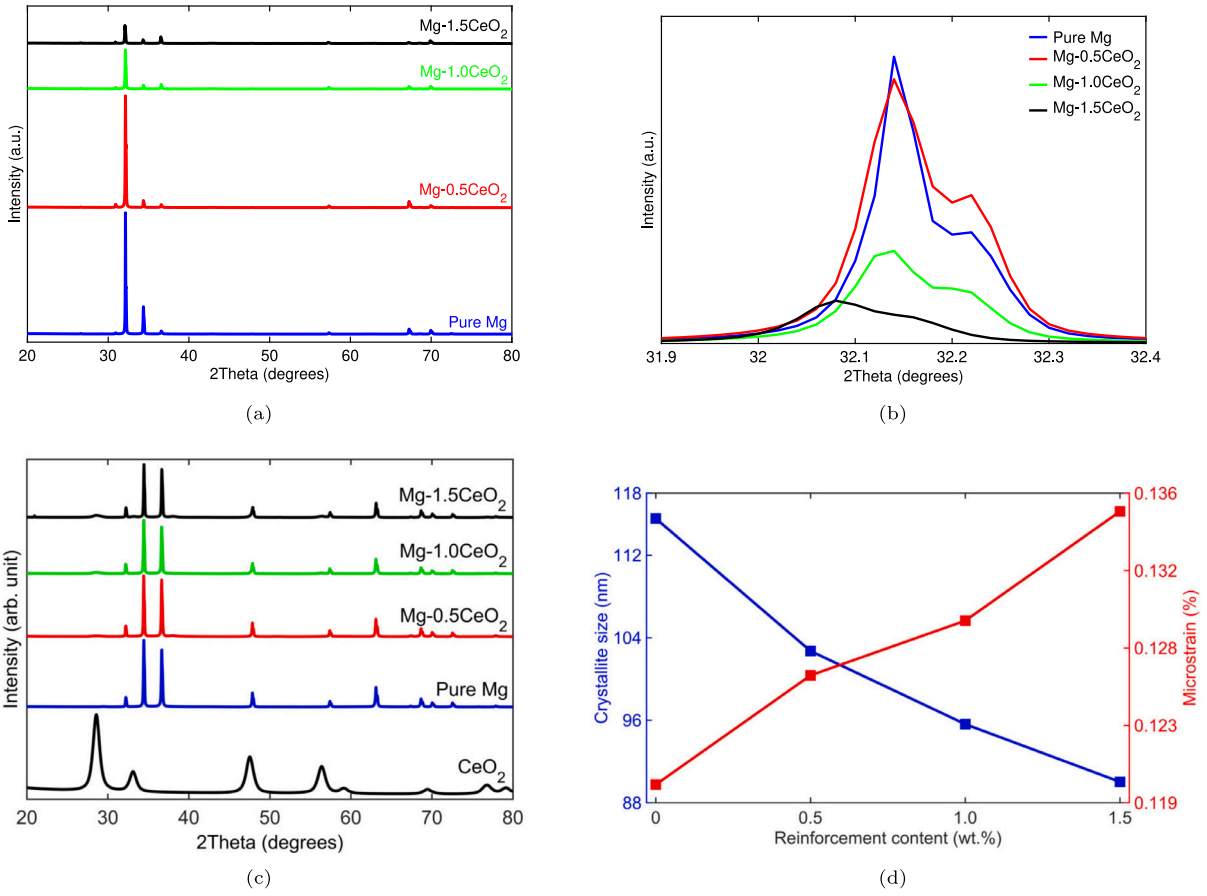

Fig. 3. (a) XRD patterns of pure Mg, Mg-xCeO_2(x = 0.5, 1 and 1.5) nanocomposites (b) XRD diffraction pattern showing peak broadening at 2θ = 32.14. The shift of the principal peak can be seen in (b), which can be due to the presence of stacking faults. (c) XRD patterns, and (d) corresponding crystallite size and microstrain variation of pure Mg, Mg-xCeO_2(x = 0.5, 1 and 1.5) nanocomposite powders.

3. Experimental results

3.1. Morphological investigations & structural evolution

The study concerning morphological and microstructural evolution of the nanocomposites is of utmost importance due to its utility in revealing various aspects, such as the agglomeration of the NPs, distribution of NPs within the matrix, grain refinement, grain growth, and micro-voids/porosity.

To synthesize high-performance CeO_2-based Mg nanocomposites, it was necessary to homogeneously distribute the second-phase particles within the Mg matrix and obtain crack-free green compacts. Following Sahed's work [28], 5 h of ball milling was done on the nanocomposite powder mixture which produced ultrafine microstructure in the samples with a uniform dispersion of reinforcements. FESEM micrographs (Fig. 2) illustrated significant changes in size and morphology of milled Mg and Mg-xCeO_2 (x = 0.5, 1, and 1.5) nanocomposite powder mixtures. The incorporation of CNPs led to flake-like particles with reduced size from 276.1 μm (Fig. 2(a)) to 60.3 μm (Fig. 2(d)). Despite uniform reinforcement distribution of CNPs, ball milling resulted in particle agglomeration. However, it was minimized in Mg-1.5CeO_2 powder mixture (Fig. 2(d)). Moreover, particle size decreased with increased reinforcement content, indicating microstructure refinement due to NP addition. This reduction in the agglomeration and particle size could be explained by the models of Benjamin [29], and Fogagnolo et al. [30]. For further insights, refer to studies by Ponhan [4] and Xiang [8].

Fig. 3 depicts the results of the XRD investigations of bulk and powdered samples of pure Mg and Mg-CeO_2 nanocomposites. From Fig. 3(a), distinct principal peaks could be noticed at 2-theta at 32°, 34°, and 37° corresponding to the hexagonal closed-pack structure (hcp) of Mg. However, the peaks of CeO_2 NPs were not detected in the nanocomposites, which corresponded to the results as explained in Refs. [31]. This was owing to the low intensity of the CeO_2 NPs due to which they failed to get detected in the XRD spectrum. Moreover, the XRD spectrum in Fig. 3(a) did not exhibit any signs of impurities or secondary phase formation, which affirmed the successful synthesis of the stable Mg-CeO_2 nanocomposites. This could be attributed to the use of PM processes at temperatures well below the melting temperatures of Mg and CeO_2. One could also detect a noticeable widening of peaks in Fig. 3(a) with an increase in the vol.% of reinforcements. It became even more prominent in the case of Mg-1.5CeO_2 nanocomposite. For better visualization, an enlarged view of the major peaks, corresponding to 2θ = 32.14, has been shown in Fig. 3(b), wherein along with the widening of the peak, a shift of the peak can also be seen. This confirms the microstructure refinement of the nanocomposites at a higher vol.% of reinforcements. The shift of the peaks could be due to the presence of the stacking faults.

As previously noted, the incorporation of NPs significantly impacts fine-tuning the microstructure of nanocomposites and must thus be thoroughly studied. Particle size reduction mentioned above directly correlates with crystallite size reduction and accumulation of lattice strain. Crystallite size and lattice strain in the nanocomposites are calculated by using the W–H method based on the XRD data of the nanocomposite powder (Fig. 3(c)). Fig. 3(d) depicts crystallite size and micro-strain values as a function of reinforcement vol.%. The crystallite size of the pure Mg and Mg-CeO_2 nanocomposite powder, as one observes in Fig. 3(d), was considerably reduced following an increase in the vol.% of the NPs and also due to the interactions between the

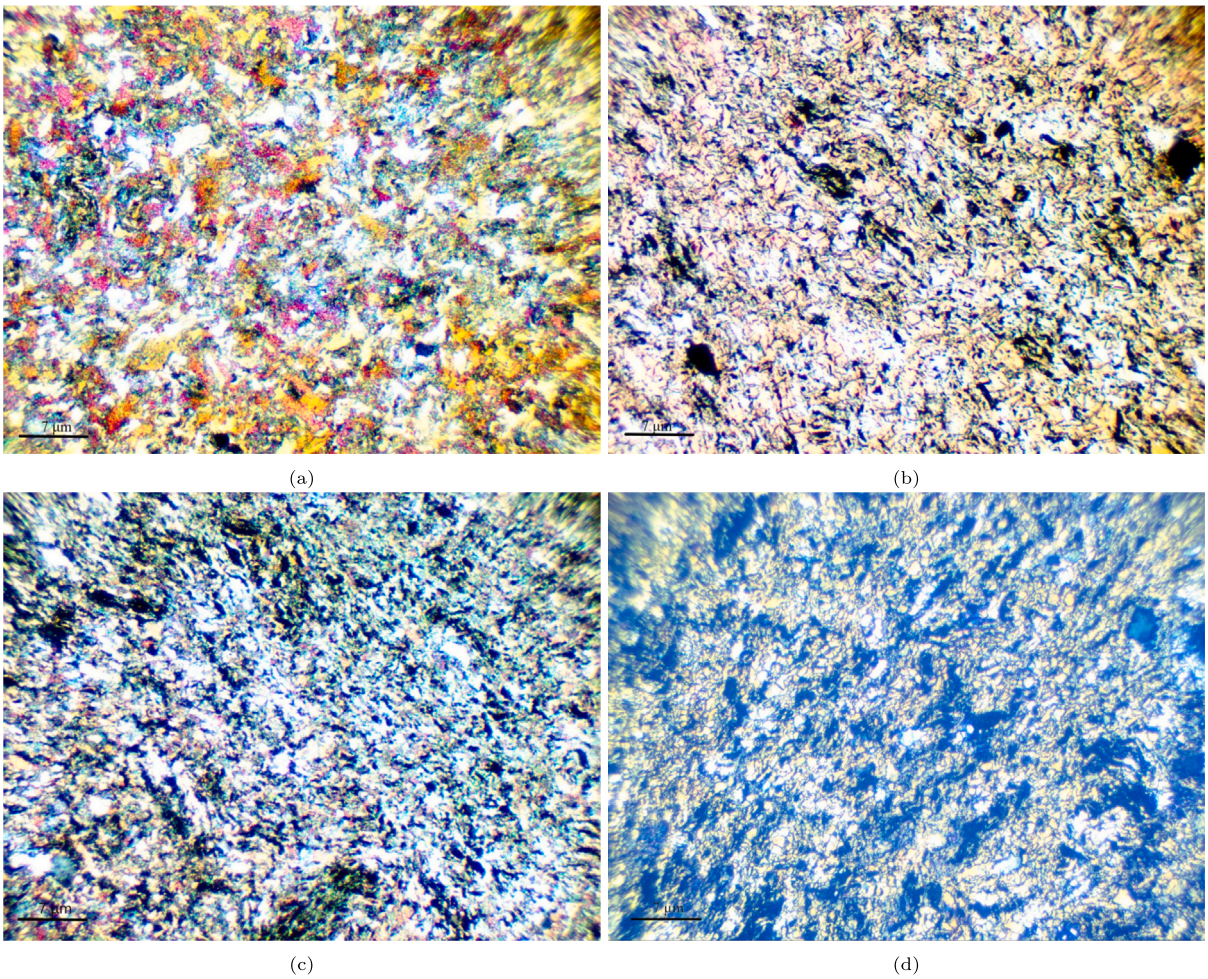

Fig. 4. Optical micrographs showing the microstructure of (a) Pure Mg, (b) Mg-0.5CeO_2, (c) Mg-1.0CeO_2, and (d) Mg-1.5CeO_2 nanocomposites.

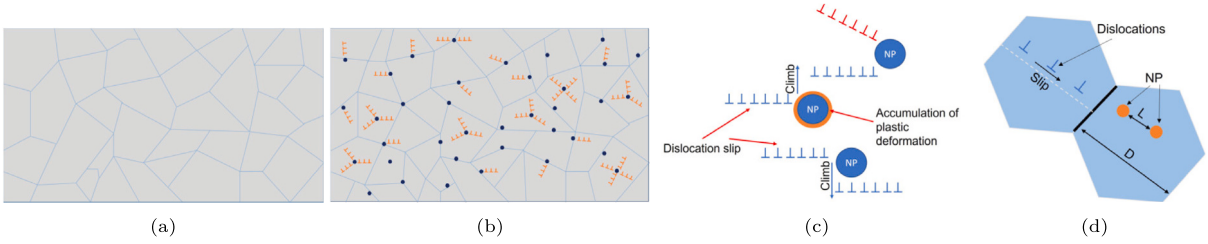

Fig. 5. Schematic illustration of the microstructure of the (a) Mg matrix, and (b) introduction of CeO_2 NPs within matrix, (c) Orowan strengthening, and (d) Grain boundary refinement; L and D represent length scale and grain size, respectively, wherein L<D.

dislocations and the reinforced NPs. During the present investigation, the average crystallite size of pure Mg, Mg-0.5CeO_2, Mg-1.0CeO_2, and Mg-1.5CeO_2 nanocomposite powder was reported to be 173.32, 163.12, 154.06, and 142.94 nm, respectively, following 5 h of high-energy ball milling. Hence, in comparison with pure Mg, one could notice a significant decrease in the crystallite size, i.e., of 5.88, 11.12, and 17.53%, for Mg-0.5CeO_2, Mg-1.0CeO_2 and Mg-1.5CeO_2, respectively. Moreover, the decrease in the crystallite size in the nanocomposite powder was accompanied by accumulation of the lattice strain. An increase in the lattice strain from 0.13 to 0.16 (approx. 23% increase) can be seen between the pure Mg and Mg-1.5CeO_2. This increase could be due to the grain refinement, brought out by mechanical attrition and reinforcement NPs [4].

Furthermore, the synthesized extruded rods of pure Mg, Mg-0.5CeO_2, Mg-1.0CeO_2 and Mg-1.5CeO_2 nanocomposites did not exhibit any sign of cracks on the surface, post extrusion. This, in turn, reiterated the feasibility of synthesizing CeO_2-based Mg nanocomposites by using PM technique (Fig. 1(b)). The optical micrographs illustrating grain refinement in pure Mg and Mg-CeO_2 nanocomposites are shown in Fig. 4. It is known that grain refinement in Mg nanocomposites plays a crucial role in strengthening and enhancing the mechanical properties of the composites and could be due to [32]: (i) Orowan strengthening due to dislocation bowing of reinforcing NPs, (ii) Hall–Petch strengthening due to microstructure refinement, (iii) Forest strengthening due to a mismatch of the coefficient of thermal expansion between NPs and matrix, and (iv) Taylor strengthening due to modulus mismatch between the matrix and the NPs. Fig. 5 illustrates a schematic representation of these strengthening mechanisms. Grain refinement is evident in Fig. 4, which shows equiaxed and uniform nature of grains in pure Mg and all the nanocomposite samples. It also demonstrates that

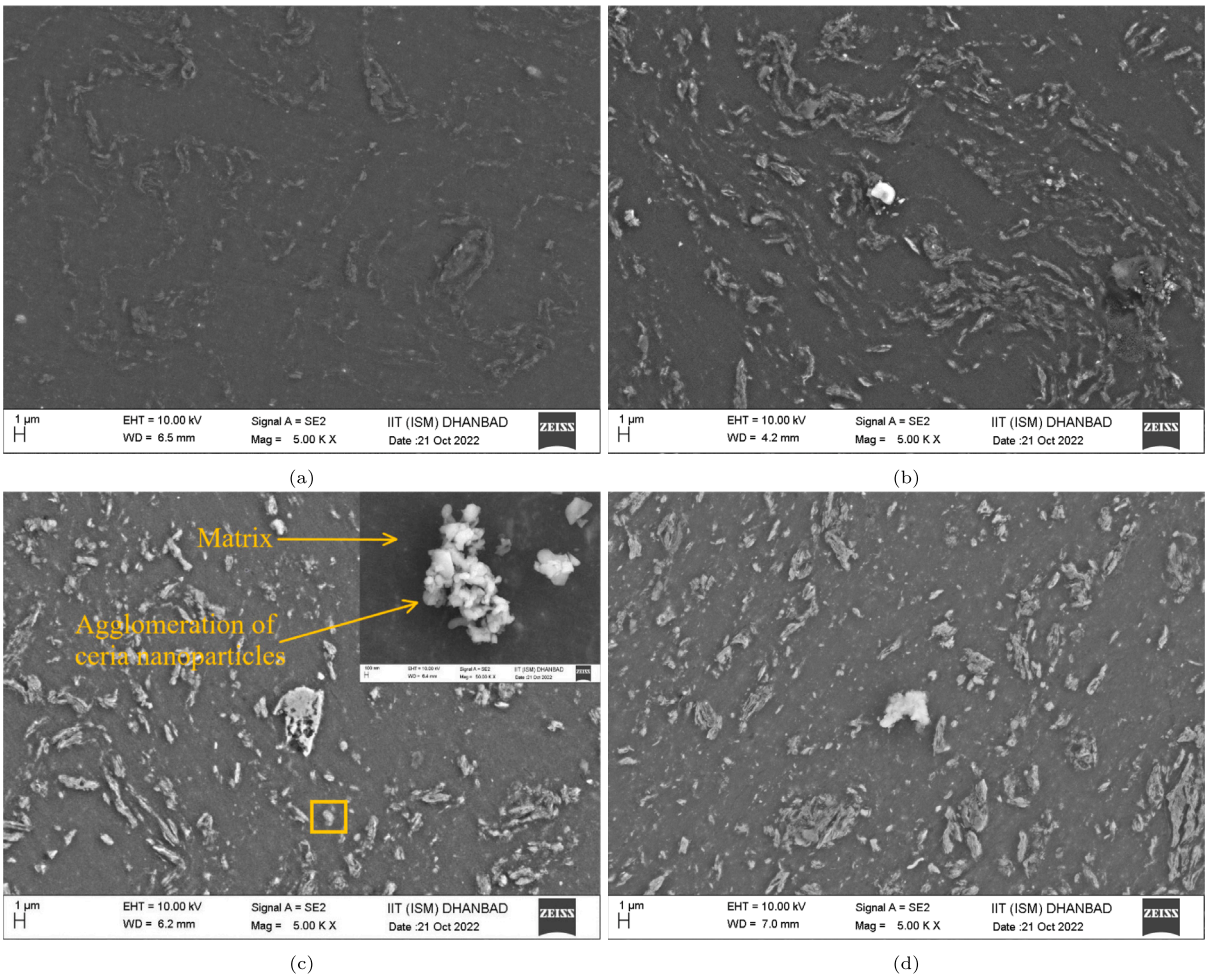

Fig. 6. Representative FESEM micrographs of (a) Pure Mg, (b) Mg-0.5CeO_2, (c) Mg-1.0CeO_2, and (d) Mg-1.5CeO_2 nanocomposites. High magnification of the yellow box mentioned in (c) showing NP agglomeration.

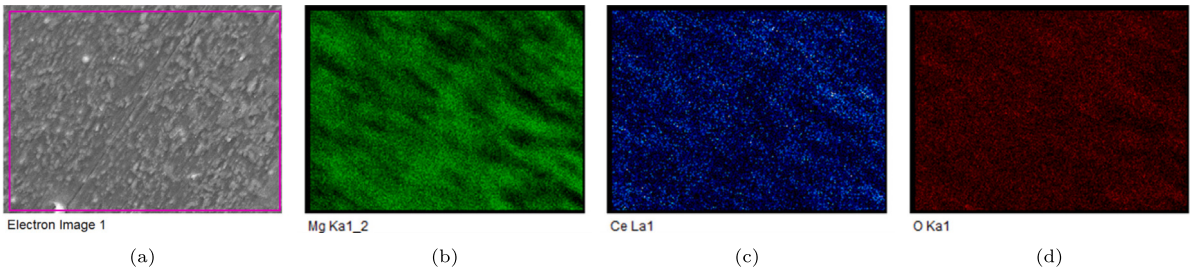

Fig. 7. FESEM-EDX analysis of Mg-1.0CeO_2 nanocomposite showing the elemental distribution of (a) original picture, (b) Magnesium, (c) Cerium and (d) Oxygen.

as the vol.% of reinforcement in the nanocomposites increased, there was a discernible reduction in the grain size of the nanocomposites when compared to pure Mg.

Microstructural analysis of the Mg-CeO_2 nanocomposite samples was done using the FESEM to identify the distribution of the CeO_2 NPs within the Mg matrix. In all the Mg-CeO_2 samples, the CeO_2 NPs were found to be uniformly dispersed throughout the matrix, as shown in Fig. 6. The bright regions in Fig. 6 correspond to the distribution of the CeO_2 NPs. The uniform distribution of NPs could be explained by two factors: (i) minimum agglomeration and homogeneous dispersion brought by mechanical attrition, and (ii) when the sintered nanocomposites billets undergone a hot extrusion process, they suffered severe plastic deformation, which in turn breaks NPs clusters and helps facilitate the transport of NPs into the matrix yielding better dispersion of NPs within the matrix. Another important aspect was minimal void contents in all the nanocomposite samples, as can be seen in Fig. 6. This could again be attributed to two factors: (i) improved reinforcement compatibility with the matrix and (ii) use of high pressure and temperature during hot extrusion. Furthermore, in order to evaluate the distribution of reinforcing nanoparticles in the nanocomposite matrix, FESEM-EDS analysis was carried out on the surface of the Mg-1.0CeO_2 nanocomposite (Fig. 7). Fig. 7 demonstrates the presence of the constituents (matrix and reinforcing element) and the uniform dispersion of CNPs throughout the nanocomposite.

The High-resolution transmission electron microscopy (HRTEM) obtained from the Mg-0.5CeO_2 nanocomposites, coupled with the selected area diffraction (SAD) pattern and energy dispersive X-ray (EDX) mapping, has been presented in Fig. 8. Fig. 8(a) depicts the formation of

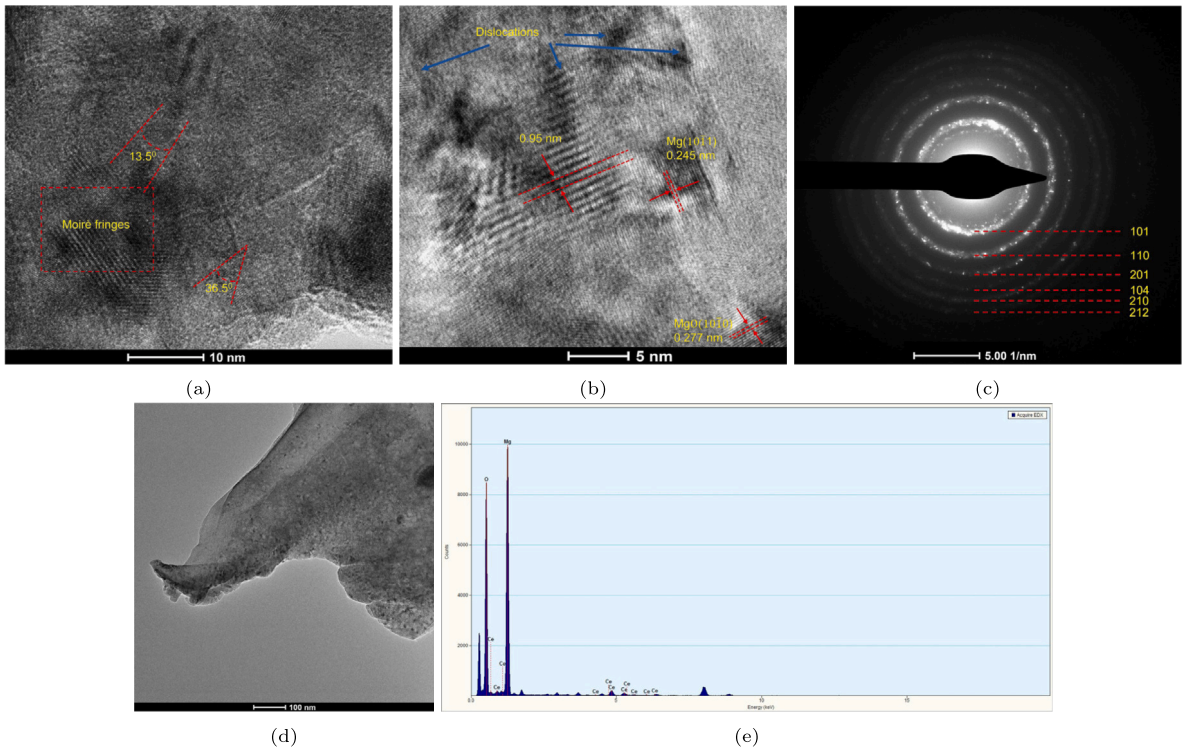

Fig. 8. HRTEM image of the Mg-0.5CeO_2 nanocomposites showing (a) Moire fringes along with low and high angle grain boundaries, (b) high-resolution image showing Mg(10$\bar{1}$1) and Mg(10$\bar{1}$0) phase, (c) associated SADP pattern of Fig. 8(b), (d) TEM micrographs of Mg-0.5CeO_2 nanocomposite showing uniform distribution of CNPs and (e) EDX mapping of the area in Fig. 8(b).

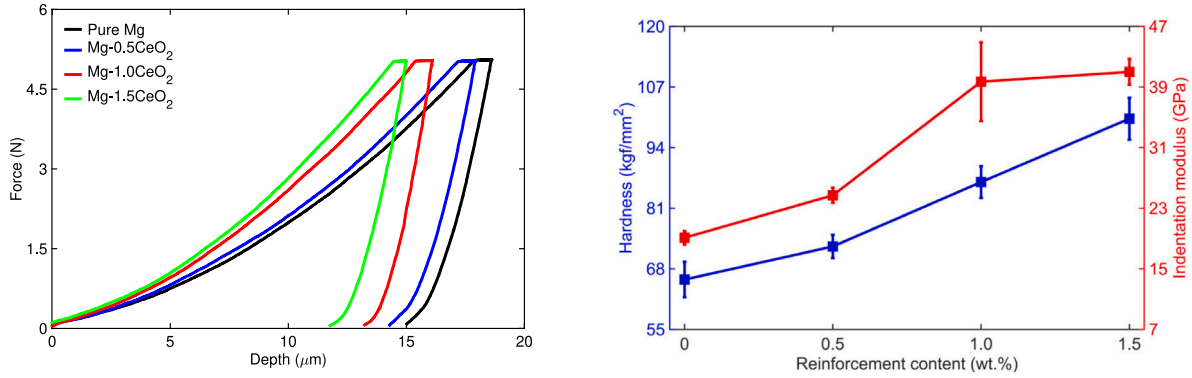

Fig. 9. (a)Force–displacement curves for pure Mg and Mg-CeO_2 nanocomposites and (b) microhardness and indentation modulus of pure Mg, Mg-CeO_2 nanocomposites.

Table 1
Density of pure Mg, Mg-CeO_2 nanocomposites.

Material	Theoretical density (g/cc)	Experimental density (g/cc)	Relative density (%)	Porosity (%)
Pure Mg	1.740	1.729 ± 0.001	99.40	0.64 ± 0.001
Mg-0.5CeO_2	1.767	1.759 ± 0.006	99.54	0.45 ± 0.006
Mg-1.0CeO_2	1.794	1.772 ± 0.003	98.80	1.22 ± 0.003
Mg-1.5CeO_2	1.821	1.786 ± 0.008	98.10	1.92 ± 0.008

moiré fringe patterns due to the superimposition of one crystal over another in the electron micrographs, thereby indicating a disparity in the lattice spacing of the crystals. Similar results regarding the moiré fringes for the Mg-SiO_2 nanocomposites were reported by Fu and his team [33]. The higher magnification image in Fig. 8(b) shows a Moiré fringe periodic spacing of 0.95 nm, as well as an Mg reflection of (10$\bar{1}$1) (d spacing= 0.275 nm) and a MgO reflection of (10$\bar{1}$0) (d spacing = 0.277 nm). Furthermore, distinctive continuous diffraction rings in the SADP pattern (Fig. 8(c)) can be seen, which could be due to the development of nano-grains. Finally, it should be pointed out that the HRTEM micrograph of Fig. 8(d) reveals a homogeneous distribution of ceria nanoparticles (CNPs) within the Mg matrix.

3.2. Density measurement

Hot extrusion-assisted PM process synthesized pure Mg and Mg-CeO_2 nanocomposite samples with near theoretical density as shown in Table 1. The improved density of the samples was possible due to

the exposure of the samples to an elevated temperature for a prolonged duration, which, in turn, caused the samples to soften and voids to get filled. Moreover, due to the application of high pressure, the samples underwent severe plastic deformation. This enabled efficient mixing of the constituents (matrix and reinforcement), minimized porosity, and improved material density. According to the results presented in Table 1, by increasing the vol.% of the NPs, the relative density of the samples decreased, and the porosity of the samples increased. This could be due to the agglomeration of the NPs with a comparable increase in their vol.% and the incorporation of hard NPS into the ductile Mg matrix [27]. For example, the relative density of Mg-1.5CeO_2 nanocomposites dropped to 98.1% from 99.4% (pure Mg) while the experimental density of Mg-1.5 CeO_2 nanocomposites showed an increase of 3.29% in comparison with pure Mg. This was due to the high density of the reinforced NPs as compared to pure Mg (Table 1 presents their density values).

Furthermore, an increase in the porosity percentage could be noted with a progressive rise in the vol.% of the NPs. Literature reports similar cases in the case of nanocomposites owing to the inherent nature of NPs to form agglomeration and, in some cases, poor interfacial integrity with the matrix [4]. The porosity percentage for pure Mg was reported to be 0.64%, while for Mg-1.5CeO_2, it was 1.92%. While the powder metallurgy products exhibited an inevitable amount of porosity, the porosity content of the fabricated pure Mg and Mg-CeO_2 samples was found to be within an acceptable limit (less than 2%), which indicated that near-dense samples were fabricated by using the proposed synthesizing process.

3.3. Microhardness measurement

Fig. 9(a) illustrates the microindentation behavior of pure Mg and Mg-CeO_2 nanocomposites with varying vol.% of CeO_2 NPs. Increasing CNP fraction resulted in a steeper force vs. displacement graph, indicating improved microhardness and indentation modulus. Fig. 9(b) shows that Mg-1.5CeO_2 exhibited a considerable increase in the hardness and indentation modulus of the matrix, which went up from 65.7 to 100.2 kgf/mm^2 (approximately 52.5% increase) and from 19.1 to 41 GPa (approximately 115% increase), respectively. The hardness of ultrafine Mg-1.5CeO_2 nanocomposites surpassed that of commercially available alloys such as AZ91, AZ31, AZ80, AZ61, and AZ81. This is due to the NPs acting as barriers, thereby bending and bypassing the dislocation around them, which causes reduced dislocation mobility and limited plastic deformation. This obstruction to the dislocation motion, in turn, increases the composite's hardness value [4,34,35].

3.4. Compression measurement

Mg and its nanocomposites have an intrinsic strain rate sensitivity, which becomes noticeable at higher temperatures. Therefore, the present study investigated the flow stress–strain curves of pure Mg and Mg-xCeO_2(x = 0.5, 1 and 1.5) nanocomposites at increased temperatures and varied strain rates to highlight the most essential and intriguing deformation properties in these nanocomposites. Additionally, in order to gain a deeper understanding of the mechanisms of deformation, the fractured surfaces were further examined by FESEM.

3.4.1. Effect of temperature

To demonstrate the temperature-dependent mechanical response of pure Mg and Mg-CeO_2 nanocomposites, the engineering stress–strain curves of this material at different strain rates of 0.01, 0.001, and 0.0001 s^{-1} have been illustrated in Fig. 10. To maintain consistency with the findings of the previously published literature, the present study based its examination on the strain rates as provided in the work of Mirza et al. [36] on rare-earth-based Mg alloy and the temperatures as provided in the work of Li et al. [37] on ultrafine Mg alloy.

As seen in Fig. 10, the flow curves behaved differently at each of the test temperatures. At room temperature (293 K), the curves exhibited linear elastic behavior followed by a substantial hardening. However, when the test temperature was increased, the hardening tendency gradually decreased. Finally, at 473 K, a nearly flat behavior characterized by a near-perfect elastic–plastic trend can be observed. This behavior resulted from a dynamic conflict between the work softening brought on by dynamic recovery and precipitation, coarsening of sub-grains, and softening of texture and the work hardening brought on by dislocation interactions, pile-up, and tangling of dislocations [38]. While this phenomenon is true for low strain rates (0.0001 s^{-1}), it becomes apparent that at higher strain rates (0.01 s^{-1}), significant hardening takes place, even when working at increased temperatures. Moreover, it can be seen that at a fixed strain rate, flow stress could be seen to reduce with the increase in temperature. While comparing the curves shown in Fig. 10, one observes that the stress–strain relationship for the monolithic Mg and the Mg-CeO_2 nanocomposites reveals a significant change in the flow stress values at temperatures ranging between 293 K and 473 K. For pure Mg, at the strain rate of 0.0001 s^{-1}, the peak compressive strength decreased by 76.12% when the temperature rose from 293 K to 473 K. However, it dropped only by 28.14% when the temperature increased from 293 K to 373 K. A maximum drop of 59.43% was seen at a strain rate of 0.001 s^{-1}, whereas a maximum drop of 39.48% was observed at a strain rate of 0.01 s^{-1}. This could be attributed to the testing at high-temperature, which triggered thermal activation, facilitating dislocation migration and reducing the stress needed to sustain deformation. Thermal activation at elevated temperatures can also assist dislocations in easily circumventing barriers caused by reinforcing particles without strongly engaging with them [39]. In addition, it is essential to note that temperature substantially affected the elongation to failure of pure Mg and nanocomposite samples. When the temperature was raised from 293 K to 473 K, pure Mg showed a maximum increase in the strain to failure by 101%, 93.97%, and 61.74%, respectively, for strain rates of 0.0001, 0.001, and 0.01 s^{-1}. For the Mg-0.5CeO_2 nanocomposites, on the other hand, the rise in elongation-to-failure was 169.76%, 126.71%, and 66.89%, respectively. Details regarding the peak compressive strength and strain-to-failure of pure Mg and Mg-CeO_2 nanocomposites have been presented in Appendix.

3.4.2. Effect of strain rate

In order to demonstrate the strain rate sensitivity of the monolithic Mg and its nanocomposites, the engineering stress–strain curves at temperatures of 293, 373, 423, and 473 K have been plotted in Fig. 11. For a given temperature, the flow stress could be seen to increase as the strain rate increased. During the present investigation, when the strain rate for pure Mg was increased from 0.0001 s^{-1} to 0.01 s^{-1} at 293 K, the UCS increased by approximately 12.9% and the FS decreased by approximately 15.06%. However, this phenomenon of increased UCS and decreased FS with increased strain rates is more apparent at 423 K. For instance, at the temperature of 423 K, with the increase in strain rate from 0.0001 to 0.01 s^{-1}, the observed increase in UCS was found to be 109.02%, 77.36%, 42.58%, and 40.72% for the Mg, Mg-0.5CeO_2, Mg-1.0CeO_2, and Mg-1.5CeO_2 nanocomposites respectively. The corresponding decrease in FS was reported as 33.27%, 37.38%, 37.22%, and 38.57% for the same nanocomposites. One can conclude from Fig. 11(b) that flow stresses increased considerably at high temperatures with the increase in the strain rates. This trend could be explained by diffusion-controlled softening processes getting activated at elevated temperatures and the reduced rate of dislocation production and shorter activation time at higher strain rates [38]. For a detailed description of the augmentation in strength and ductility of all nanocomposites at temperatures of 293, 373, 423, and 473 K and strain rates of 0.0001, 0.001, and 0.01 s^{-1}, please refer to Appendix (see Fig. 12).

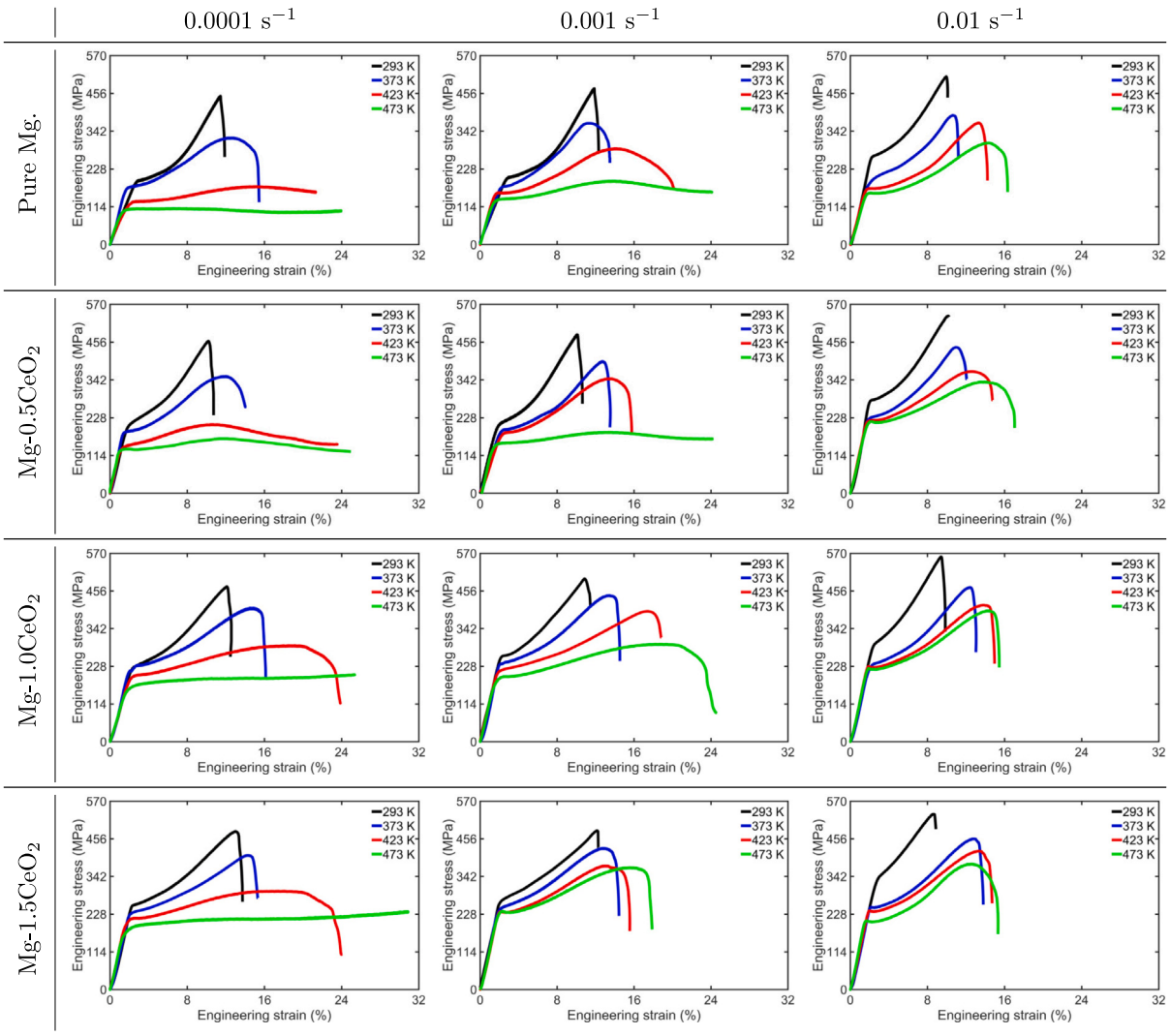

Fig. 10. Engineering stress–strain curves of pure Mg and Mg/CeO_2 nanocomposites at elevated temperatures of 293–473 K under strain rates of 0.0001 s^{-1}, 0.001 s^{-1}, and 0.01 s^{-1}.

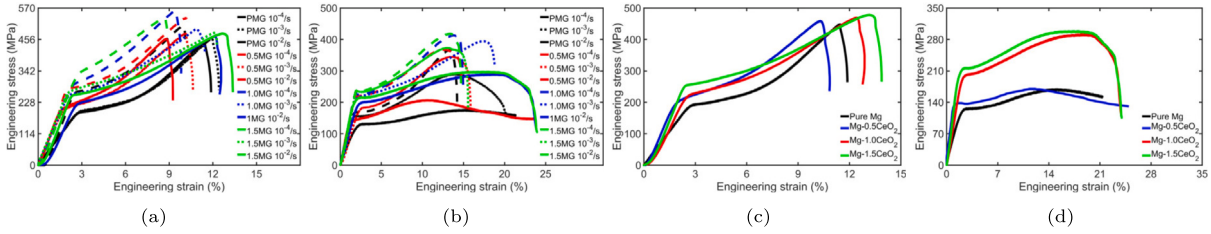

Fig. 11. Effect of strain rate on the compressive behavior of pure Mg and Mg-CeO_2 nanocomposite at temperatures of (a) 293 K, and (b) 423 K. Effect of reinforcement content on the compressive behavior of pure Mg and Mg-CeO_2 nanocomposite at temperatures of (c) 293 K, and (d) 473 K. PMG means pure Mg, 0.5MG means Mg-0.5CeO_2, 1.0MG means Mg-0.5CeO_2, and 1.5MG means Mg-1.5CeO_2.

3.4.3. *Effect of reinforcement content*

The compression test results at room temperature and elevated temperature, as shown in Fig. 11 demonstrate that the addition of ceramic NPs to the Mg matrix enhanced the material's compressive yield strength (CYS), UCS, and FS. The values of CYS and UCS of the nanocomposites were significantly greater than those of the monolithic matrix samples along the entire range of the test temperatures. However, the difference was most pronounced at 423 K. The strain rate during the observation, as presented in Figs. 11(c) and 11(d), was 0.0001 s^{-1}. At 423 K, the CYS of the monolithic Mg was 130.18 MPa, while Mg-1.5CeO_2 had the highest CYS at 213.63 MPa among the three nanocomposites (an improvement of 64.10% over pure Mg). A variety of strengthening factors could explain this trend, including the Orowan strengthening mechanism resulting from the reinforcement's restriction of dislocation movement [12,39], the thermal and elastic moduli mismatch between the matrix and reinforcement, which increases dislocation density and thereby increases strength [12](CTE of Mg =27.1 × 10^{-6} K^{-1} [12]; CTE of CeO_2 = 10.6 × 10^{-6} K^{-1} [12]), the strong bonding between the reinforcement and the matrix, and adequate load transfer between the matrix and reinforcement [40]. It could also be due to the refined microstructure of the samples facilitated by CNPs and high-energy ball milling, which reduces the dislocation

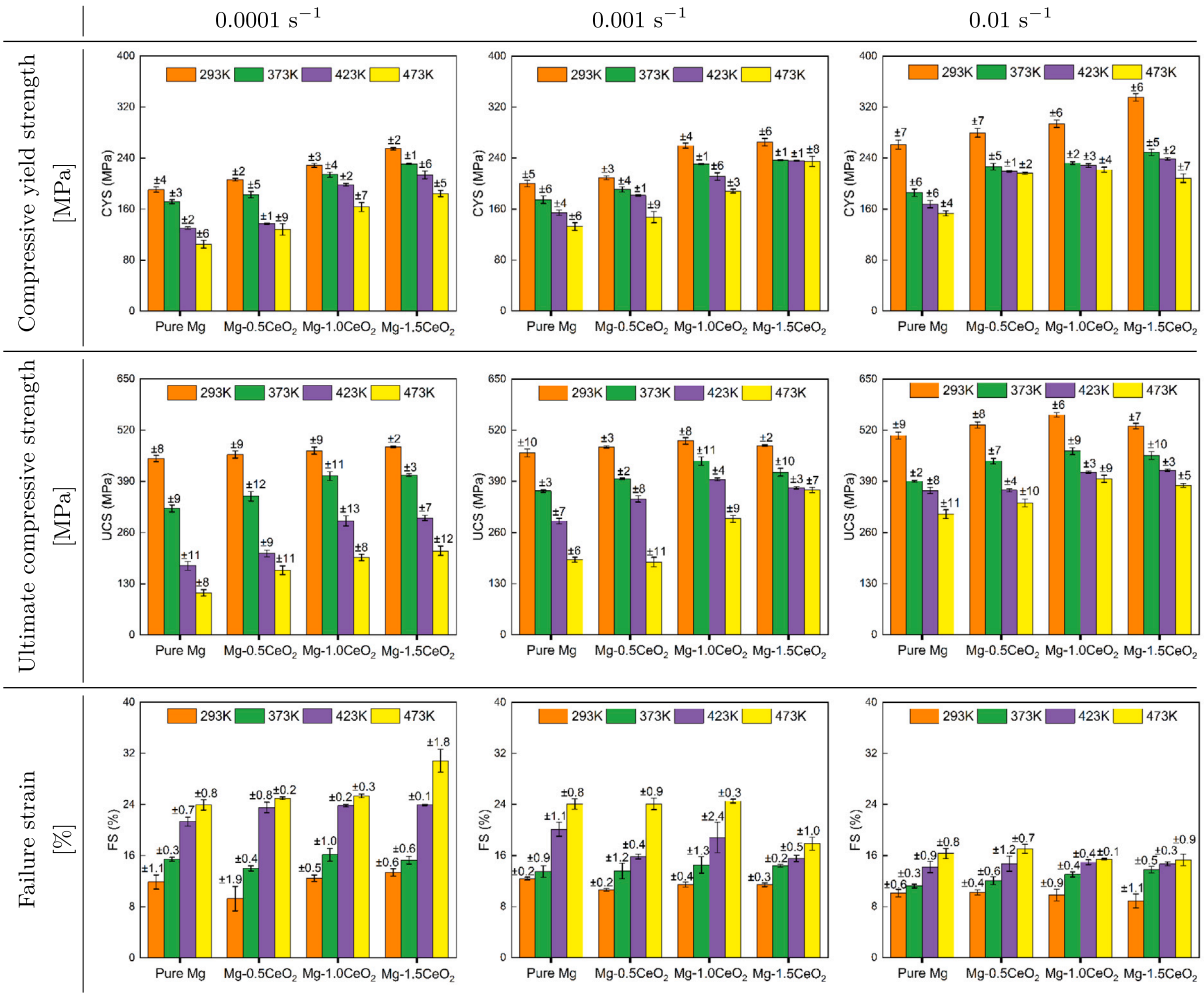

Fig. 12. Summary of the compression properties of monolithic Mg and Mg-xCeO_2(x = 0.5, 1, and 1.5) nanocomposites at different test temperatures and strain rates. Please refer to the Appendix for more details.

mean travel distance and causes dislocation accumulation at grain boundaries, leading to strength improvement in the nanocomposite samples [38]. In Fig. 11(c), one could notice that all the nanocomposite samples had increased FS as compared to the unfilled matrix. The only exception was the Mg-0.5CeO_2 sample, which had a lower FS in comparison with the pure Mg. Mg-1.5CeO_2 exhibited the maximum strain to failure of 13.36%, which was 13% more than that of pure Mg. The improvement in the FS could be attributed to the activation of the non-basal slip systems in the matrix due to the CNPs. This also underlines that the reinforcement agglomeration was minimized by utilizing the powder metallurgy production method. The augmentation of FS could also be credited to the presence and uniform dispersion of CNPs within the Mg matrix [41]. Previous research established that the NPs help create sites for the advancing crack front where cleavage cracks could be opened, dissipating the stress concentration that might otherwise exist at the crack front and modifying the local effective stress state in the area of the crack tip. Please refer to Table 2 for comparing the mechanical characteristics of Mg-CeO_2 nanocomposites to particular Mg-based nanocomposites and commercial Mg alloys.

In a macroscopic sense, failure occurred for the majority of samples at 45 degrees to the compression loading axis when tested at room temperature or at higher strain rates. However, when the samples were subjected to elevated temperatures and slower strain rates, the coining of the samples happened due to a softening or mushing effect at elevated temperatures. Next, Fig. 13 illustrates the FESEM fractography of pure Mg and Mg-CeO_2 nanocomposite samples under compression at 293 K, 373 K, 423 K, and 473 K. The first column in Fig. 13 demonstrates the fractography of monolithic Mg and Mg-xCeO_2 (x = 0.5, 1.0, and 1.5 vol.%) nanocomposites at room temperature. From the first column, it is evident that all the specimens failed by the shear mode of fracture in the presence of varied degrees of shear bands. Moreover, no substantial dimples or cleavage platforms on the fractured surface could be observed in the fractography. In addition, there were a few microvoids and micro fractures along the shear bands, indicating that one of the failures experienced by the samples might be associated with the generation and spread of the microvoids. In the 3rd and 4th columns of Fig. 13, which corresponded to the compression at 423 K and 473 K, the fractography shows dimples, cleavage features, and clear slip lines, suggesting a more ductile response. Similar observations about the nature of fractures were reported in studies by Yun et al. Chen et al. [54], and Meenashisundaram, et al. [47]. In conclusion, the features of the fracture surfaces were in line with the amount of ductility shown by the stress–strain curves in Fig. 10. It is important to note that for all the three static strain rates at 473 K temperature, the samples of monolithic Mg and Mg-0.5CeO_2 failed to break into two pieces due to softening of the samples. Thus, the third and fourth rows in Fig. 13 do not have a matching Fig. d. However, the samples of Mg-1.0CeO_2 and Mg-1.5CeO_2 fractured at 473 K at the strain rate of 0.01 s^{-1} although they failed to do so at the strain rates of 0.0001 and 0.001 s^{-1}.

Table 2
Compression properties of Mg, its alloys and nanocomposites.

Material	Processing method	Hardness (kgf/mm^2)	0.2% offset YS (MPa)	UCS (MPa)	Fracture strain (%)	Reference
Pure Mg	PM (with MM)	65 ± 3.8	261 ± 7	506 ± 9	10.09 ± 0.6	Present study
Mg-0.5CeO_2	PM (with MM)	72 ± 2.5	279 ± 7	533 ± 8	10.21 ± 0.4	Present study
Mg-1.0CeO_2	PM (with MM)	86 ± 3.4	294 ± 6	559 ± 6	9.81 ± 0.9	Present study
Mg-1.5CeO_2	PM (with MM)	100 ± 4.5	335 ± 6	530 ± 7	8.87 ± 1.1	Present study
Mg-1.5CeO_2	PM (without MM)	75 ± 2.4	111 ± 2	329 ± 7	19.7 ± 0.8	[12]
Mg-0.5Zn-1.5CeO_2	PM (without MM)	96	135 ± 1	420 ± 1	17.4 ± 0.9	[6]
Mg-0.3BN	DMD + HE	NR	70 ± 8	234 ± 8	20.7 ± 0.9	[42]
Mg-0.8AlN	PM + MW + HE	NR	71 ± 3	307 ± 17	18.3 ± 2.3	[43]
Mg-1.11B_4C	PM + MW + HE	NR	105 ± 3	331 ± 10	13.3 ± 1.4	[44]
Mg-1.1Al_2O_3	DMD	65.9 ± 0.9	175 ± 3	246 ± 3	14 ± 2.4	[45]
Mg-1.0SiC	PM + MW	43.2 ± 2	157 ± 22	203 ± 22	7.6 ± 1.5	[46]
Mg-2.5TiO_2	DMD + HE	68 ± 1.5	101 ± 9	305.5 ± 11	22 ± 2	[47]
Mg-5.0WO_3	PM	53	NR	149.17	0.45	[48]
Mg-1.0Ni-CNT	PM	NR	454	504	10.5	[49]
AZ91D-CNT	DMD	NR	272	412	24.4	[50]
WE54	NA	NR	210	325	27	[6]
AM50	NA	NR	110	312	11.5	[6]
AZ91	SPS	76.9 ± 1.2	156.4 ± 3.3	354.2 ± 13.3	17 ± 2.2	[51]
ZK60	Casting	NR	289	425	13	[52]
AZ91D	NA	NR	130	300	12.4	[6]
AZ31	CR	NR	125	352	16.8	[53]

Note: PM = powder metallurgy; MM = mechanical milling; DMD = disintegrated melt deposition; HE = hot extrusion; MW = microwave sintering; NR = not reported; SPS = spark plasma sintering; CR = cold rolling.

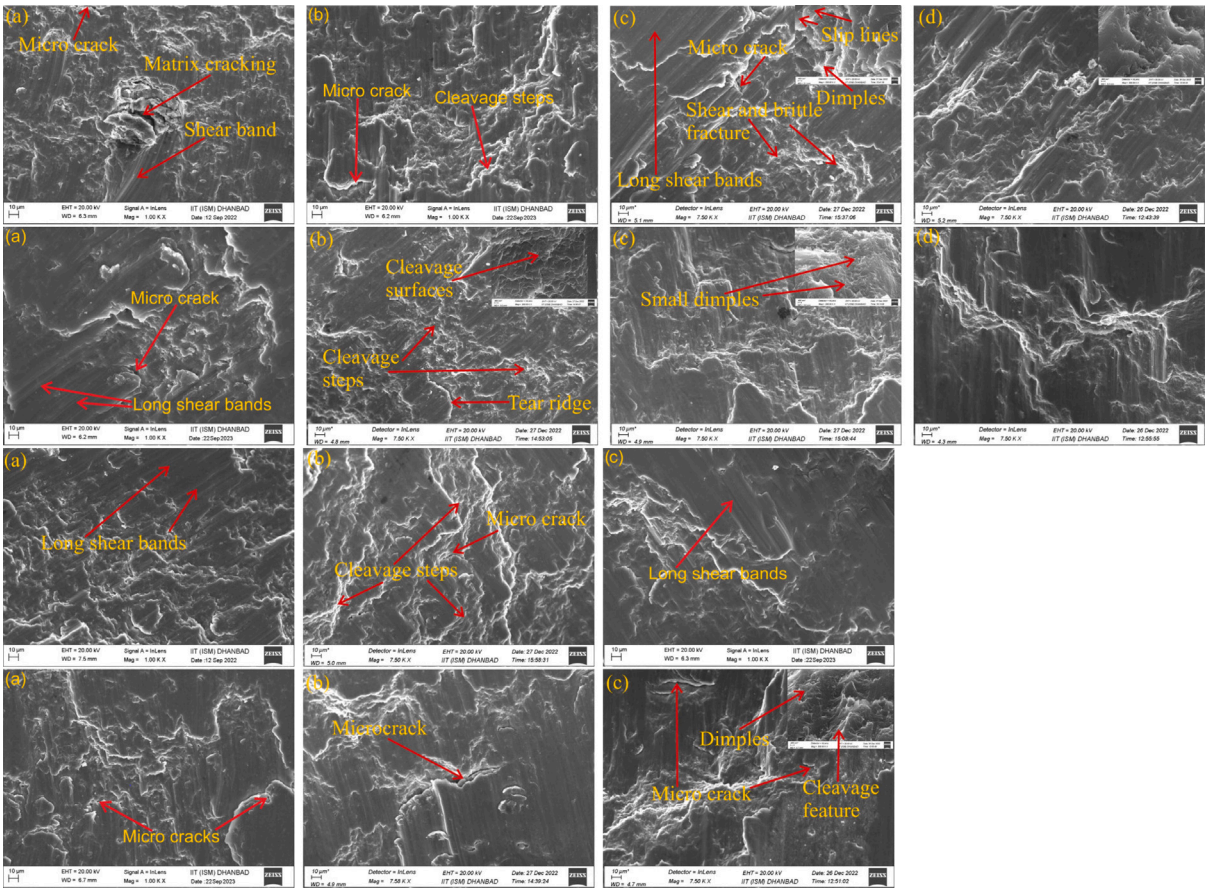

Fig. 13. FESEM compressive fracto-graph of pure Mg and Mg-CeO_2 nanocomposites at different temperatures. The first row of micrographs corresponds to Mg-1.5CeO_2 nanocomposites with (a–d) represented at temperatures of 293 K, 373 K, 425 K, and 473 K, respectively. Second, third and 4th row of micrographs correspond to Mg-1.0CeO_2, Mg-0.5CeO_2, and monolithic Mg with (a–d) represents the same meaning as mentioned above. The insets represent the high-magnification images of the corresponding micrographs.

3.5. Primary strengthening mechanisms

Four primary mechanisms have been discussed which are primarily responsible for the improvement of the strength of particle-reinforced MMNC [32]: (i) Orowan strengthening due to Orowan bowing of dislocations in order to bypass the NPs, (ii) Hall–Petch strengthening by refinement of grains, (iii) Taylor strengthening caused by a mismatch of the Coefficient of Thermal Expansion (CTE) and elastic

modulus between the matrix phase and NPs, and (iv) load strengthening mechanism by means of load transfer from the matrix to the reinforcement.

Theoretically, to increase the strength and ductility of MMNCs, the Orowan strengthening process is recommended. The Orowan method is suitable for the MMNCs, especially Mg MMNC because distributed second-phase nanoscale sized particles could offer significant strength improvement without necessarily reducing ductility. In other words, the Orowan mechanism typically plays an essential role in enhancing the YS of the composites due to the incorporation of the NPs. Therefore, the application of the Orowan strengthening mechanism is the most effective in hexagonal-close-packed (HCP) Mg nanocomposites. Based on Orowan–Ashby equations, the YS can be expressed as follows [55]:

$$\Delta\sigma_{\text{Orowan}} = \beta \frac{0.4Gb}{\pi\sqrt{1-\upsilon}} \frac{\ln(\bar{d}/b)}{\lambda} \tag{1}$$

where β is a constant; υ, G, and b represent the Poisson's ratio, shear modulus of Mg matrix, and burger vector, respectively; $\bar{d} = \sqrt{2/3}d_p$, where d_p is the diameter of the reinforced NPs; λ represents inter-particle spacing and is expressed by the following equation, $\lambda = \bar{d}\left(\sqrt{\pi/4\upsilon_p} - 1\right)$ where υ_p represents the volume fraction of reinforcements.

In addition to Orowan strengthening mechanism, grain refining also increased the strength of Mg MMNCs. Grain refinement in Mg MMNCs can be accomplished by mechanical alloying, post-processing, and by the inclusion of the NPs. It was established that grain refinement happens when reinforcement in considerable quantity is added to the matrix. This behavior results from the prevalence of grain border pinning, which stops the growth of grains. The Hall–Petch relationship, which is used to compute the increase in YS by means of grain refining, has been expressed by the following equation [55]:

$$\Delta\sigma_{\text{Hall–Petch}} = K\left(d_c^{-\frac{1}{2}} - d_m^{-\frac{1}{2}}\right) \tag{2}$$

where d_c and d_m are the average grain size of the composite and matrix, respectively, and K is the Hall–Petch slope.

The Taylor relationship correlates to the effect of dislocation density on the material strength. These dislocations are the byproduct of the residual plastic strain, resulting from a mismatch of elastic modulus and coefficient of thermal expansion between the matrix and reinforcement or by strain hardening in extrusion. The general equation for the impact of thermal mismatch on the nanocomposite's strength is formulated by [55]

$$\Delta\sigma_{CTE} = \sqrt{3}\beta Gb\sqrt{12\frac{\Delta\alpha\Delta T\upsilon_p}{\left(1-\upsilon_p\right)bd_p}} \tag{3}$$

where $\Delta\alpha$ is the thermal expansion coefficient differential between the CeO_2 NPs and the Mg matrix; ΔT represents the difference between the processing temperature and the testing temperature.

The load can be carried efficiently from the Mg matrix to the CeO_2 NPs, which also enhances the strength. The following formulation could be used to determine the contribution of strength in the load transfer effect in the particle-reinforced MMNCs by using the modified Shear Lag model [55]

$$\Delta\sigma_{load} = 0.5S\upsilon_p\sigma_m \tag{4}$$

where S represents the aspect ratio of the NPs, and σ_m represents the YS of the matrix.

Hence, the contribution of the individual strengthening mechanisms with regard to the YS of the Mg-CeO_2 nanocomposites could be established, enabling a better understanding of the mechanisms and ultimately leading to enhanced nanocomposite strength. The parameters were used to calculate YS improvement are $\beta = 1.25$, $G_m = 17.3$ GPa, $E_m = 45$ GPa, $\upsilon = 0.3$, b = 0.35 nm, K = 0.13, $\Delta\alpha = 16.5\times10^{-6}K^{-1}$, $\Delta T = 300$ K, S = 1, $d_p = 70$ nm and $\sigma_m = 190.53$ MPa [55,56]. The literature acknowledges using three superposition approaches—arithmetic summing, quadratic summation, and compounding method—to evaluate the strength enhancement of particle-reinforced MMNCs. In this regard, it may be helpful to refer to the work of Kim et al. [56] on Mg-based nanocomposites, which demonstrated that while compounding and quadratic methods occasionally succeeded in predicting the YS of the nanocomposites, they failed to do so in most of the cases. In contrast, the method of arithmetic summation displayed much better overall performance. As a result, for the present investigation, the arithmetic summation methodology was applied to predict the YS of Mg-CeO_2 nanocomposites.

$$\Delta\sigma_c = \Delta\sigma_{\text{Orowan}} + \Delta\sigma_{\text{Hall–Petch}} + \Delta\sigma_{\text{CTE}} + \Delta\sigma_{\text{Load}} \tag{5}$$

where $\Delta\sigma_c$ represents the improvement in the theoretical YS of the nanocomposite. The contribution of strengthening mechanisms for Mg/1.0CeO_2 nanocomposite: $\Delta\sigma_{\text{Orowan}} = 13.06$ MPa, $\Delta\sigma_{\text{Hall–Petch}} = 21.45$ MPa, $\Delta\sigma_{\text{CTE}} = 70.08$ MPa, $\Delta\sigma_{\text{Load}} = 0.95$ MPa and $\Delta\sigma_c = 105.53$ MPa, whereas for Mg/1.5CeO_2 nanocomposite: $\Delta\sigma_{\text{Orowan}} = 16.48$ MPa, $\Delta\sigma_{\text{Hall–Petch}} = 44.28$ MPa, $\Delta\sigma_{\text{CTE}} = 86.04$ MPa, $\Delta\sigma_{\text{Load}} = 1.42$ MPa and $\Delta\sigma_c = 148.21$ MPa. Hence, the theoretical YS of Mg-1.0CeO_2 and Mg-1.5CeO_2 nanocomposites was estimated to be 296.06 MPa and 338.74 MPa, respectively, which agreed well with the measured values of 294.02 MPa and 335.21 MPa (at the temperature of 293 K and strain rate of 0.01 s^{-1}). Therefore, one could conclude that dislocation strengthening, Hall–Petch, and Orowan strengthening methods significantly contribute to the enhanced strength of the Mg-CeO_2 nanocomposites. Kim and his co-authors [56] reported similar results on the contribution of the strengthening mechanisms to the YS of the Mg-based nanocomposites.

4. Mathematical modeling

4.1. Johnson–cook constitutive model

This section presents the J–C constitutive model to explain the plastic response of the Mg-CeO_2 nanocomposites. The J–C constitutive model is built in a paired manner in which the strain rate sensitivity, the isotropic strain hardening and the thermal softening are represented as follows:

$$\bar{\sigma} = \left[A + B\varepsilon_{pl}^{n}\right]\left[1 + C\ln\left(\frac{\dot{\bar{\varepsilon}}}{\dot{\bar{\varepsilon}}_0}\right)\right]\left[1 - \left(\frac{T - T_r}{T_M - T_r}\right)^m\right] \tag{6}$$

where $\bar{\sigma}$ is the flow stress, $\dot{\bar{\varepsilon}}_0$ is the reference strain rate, $\dot{\bar{\varepsilon}}$ is the applied strain rate, T is the applied temperature, T_r is the reference temperature, T_M is the melting temperature, and A, B, n, C, m are material constants. By fitting the true stress–strain curves at various strain rates and assessed temperatures these material constants could be determined. In addition, the reference strain rate and reference temperature were chosen as 0.0001 s^{-1} and 293 K, respectively.

4.1.1. Parameter calibration

In order to determine the parameters of the J–C model, the stress–strain curves were fitted at various strain rates and temperatures. The following procedure was conducted to determine the material constants in pure Mg and Mg-CeO_2 nanocomposites.

• *Determining parameters A, B and n:*

When $\dot{\bar{\varepsilon}} = \dot{\bar{\varepsilon}}_0 = 0.0001$ s^{-1} and $T = T_r = 293$ K, Eq. (6) can be formulated as

$$\bar{\sigma} = \left[A + B\varepsilon_{pl}^{n}\right] \tag{7}$$

where A represents the YS at the reference rate, B is the strain hardening parameter, and n is the strain hardening exponent. By taking the logarithm on both sides of Eq. (7) and rearranging yields

$$\ln(\bar{\sigma} - \text{A}) = \text{n}\ln\varepsilon_{\text{pl}} + \ln\text{B} \tag{8}$$

Table 3
J–C parameters of pure Mg, Mg-CeO_2 nanocomposites.

Material	A (MPa)	B (MPa)	n	C	m
Pure Mg	190	6413.18	1.46	−0.0017	0.580
Mg-0.5CeO_2	206	7243.23	1.56	−0.0027	0.711
Mg-1.0CeO_2	228	7785.28	1.62	−0.0253	0.760
Mg-1.5CeO_2	255	9782.91	1.51	−0.0317	0.637

Therefore, the curve between $\ln(\bar{\sigma} - \mathrm{A})$ and $\ln \varepsilon_{\mathrm{pl}}$ is a linear curve fitting where the slope equals n, and the intercept provides the value of B, $B = \exp(intercept)$. The values of A, B, and n for pure Mg and Mg-CeO_2 nanocomposites have been summarized in Table 3.

• *Determining parameter C:*

Next, in order to find the strain rate hardening co-efficient C, $T = T_r$ was initialized, which, in turn, led to the formulation of Eq. (6) as

$$\bar{\sigma} = \left[A + B\varepsilon_{pl}^{n}\right]\left[1 + C\ln\left(\frac{\dot{\bar{\varepsilon}}}{\dot{\bar{\varepsilon}}_0}\right)\right] \tag{9}$$

Considering $\dot{\bar{\varepsilon}}^* = \ln(\frac{\dot{\bar{\varepsilon}}}{\dot{\bar{\varepsilon}}_0})$ and rearranging Eq. (9) results into

$$\frac{\bar{\sigma}}{(A + B\varepsilon^n)} = \left(1 + C\ln\dot{\bar{\varepsilon}}^*\right) \tag{10}$$

Therefore, in order to estimate the parameter C, the slope of the linear curve fitting between $\frac{\bar{\sigma}}{(A+B\varepsilon^n)}$ and $\left(C\ln\dot{\bar{\varepsilon}}^*\right)$ with an intercept of 1 was computed for strain rates of 0.01, 0.001, and 0.0001 s^{-1}.

• *Determining parameter m:*

When the applied strain rate is the reference strain, i.e., $\dot{\bar{\varepsilon}} = \dot{\bar{\varepsilon}}_0$, Eq. (6) can be rewritten as

$$\bar{\sigma} = \left[A + B\varepsilon_{pl}^{n}\right]\left[1 - \left(\frac{T - T_r}{T_M - T_r}\right)^{m}\right] \tag{11}$$

Here, the strain rate strengthening effect was not taken into account. Considering $T^* = \frac{T-T_r}{T_M-T_r}$, taking the logarithm and rearranging Eq. (11) yields

$$\ln\left[1 - \frac{\sigma}{(A + B\varepsilon^n)}\right] = m\ln T^* \tag{12}$$

Consequently, the material constant, m, may be estimated based on the slope of the fitted curve between $\ln\left[1 - \frac{\sigma}{(A+B\varepsilon^n)}\right]$ and $\ln T^*$ using the linear curve fitting technique. Table 3 summarizes calibrated J–C parameters for the synthesized monolithic Mg and the Mg-CeO_2 nanocomposites. A comparative study of the J–C parameters could be attempted by referring to the work of Wang et al. [57] on Mg.

4.2. Machine learning-assisted modeling

This section proposes developing an ANN-based machine learning approach to predict the rate- and the temperature-dependent response of Mg-CeO_2 nanocomposites. ANN, as biologically inspired computational networks, use weights and biases to determine the correlation between input and target values. For the present study, the multilayer perceptrons (MLPs) network with back-propagation learning algorithms was applied as one of the versatile ANN settings for various problems. It was based upon a supervised learning procedure and comprised three layers: input, hidden, and output.

4.2.1. Data preparation

There is a general consensus that the number of samples for training a network, which depends on the complexity of the problem and the adopted algorithm, significantly influences the MLP performance [58]. To this end, a total of $1,614,590$ samples was used to train the proposed network by splitting them into three disjointed sets for training, verification, and testing in ratios of 70%, 15%, and 15%, respectively. By having the architectures of the MLP and identifying the influential input variables, MLP is trained through the training stage by supplying the input variables and comparing the output values with the target values. The training stage proceeded by continuously refining weight coefficients between the layers until the convergence criterion was satisfied. The well-trained network performance was then re-evaluated by a new data set to verify its accuracy and re-adjusted weights and biases. Finally, a separate set of data was supplied to the MLP to test the setting after completing the training and verification stage. The input data set was randomly shuffled to ensure that the training, test, and validation sets genuinely represented the overall distribution of the data and achieved higher generalization levels. Randomly shuffling training data sets could ensure an efficient learning process by improving the testing accuracy and achieving a higher rate of convergence [59].

Furthermore, data normalization is an essential preprocessing operation in which input and output variables are mapped within the same range of values, significantly influencing the network training efficiency and accuracy [60,61]. The dispersion of the CeO_2 NPs in unit volume is denoted as volume fraction, and strain values within the range of $[0, 1.5]$ and $[0, 0.4]$, respectively, are supplied to the network without further normalization. The strain rate values and temperature were fed to the network as $\ln(\dot{\varepsilon})$ and T/T_r within a range of $[-9.2, -4.6]$ and $[0, 0.37]$, respectively. Stress values were normalized using the relation σ/σ_{max} within the range of $[-1.5e^{-4}, 1]$, leading to a straightforward mapping back process to determine non-normalized stress values.

4.2.2. Network architecture

Experimental data collected from the compression tests established that four parameters, i.e., volume fraction, strain, strain rate, and temperature, significantly affected the mechanical response of the monolithic Mg and Mg-CeO_2 nanocomposites. Sensitivity to the above-referred parameters necessitated considering one input layer $\in \mathbb{R}^4$ with four independent input features. The proposed MLP also comprised two hidden layers, i.e., $\in \mathbb{R}^{20}$, and one output layer, $\in \mathbb{R}^1$, ensuring the most computationally optimal performance, that is, the best balance between the accuracy of the solution and the computational time. Fig. 14 illustrates the architecture, which was developed for the MLP network with a back-propagation learning algorithm. Here, hidden layers used a hyperbolic tangent sigmoid transfer function, which mapped the inputs within the range of $(-1, 1)$. The output layer employed a linear (or identity) transfer function as the most commonly used activation function for the output layers. The Bayesian regularization back-propagation algorithm was proposed for training the present network. It significantly minimized the propensity for over-fitting and provided a better generalization [62,63].

Figs. 15a–c show the regression analysis for three training, testing, and validation data sets disjointedly extracted from the whole number of samples. Furthermore, the coefficient of determination was employed to measure the accuracy of the fitting. In the figures, $r = 1$ signifies that the fitting ensures 100 percent variability of the data. From Figs. 15a–c, a good correlation between the predicted and the targeted values could be established with the r value being close to 1 for all cases. Fig. 15(d) presents the performance of the proposed network in terms of the Mean Square Error (MSE). It turned out that the MSE decreased with an increasing number of epochs, which ensures sufficiently converged results. The best training performance was $-7.5851e^{-6}$ at epoch 1000. Here, epoch refers to the number of passing around the whole data set in the network.

4.3. Mechanical response predictions

Here, both the J–C constitutive model and the MLPs network with back-propagation learning algorithms were used to predict the rate- and temperature-dependent response of the monolithic Mg and Mg-CeO_2 nanocomposites. The models were validated by comparing them to the experimental data for various volume fractions, strain rates, and temperature cases.

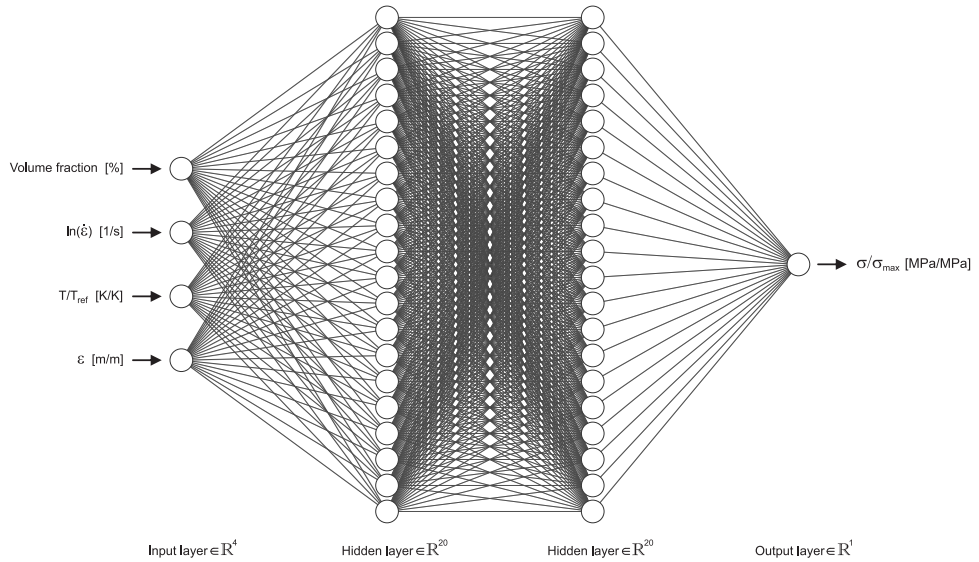

Fig. 14. The architecture of the multilayer perceptrons with a back-propagation network employed for predicting the rate- and temperature-dependent flow behavior of monolithic Mg and Mg-CeO_2 nanocomposites.

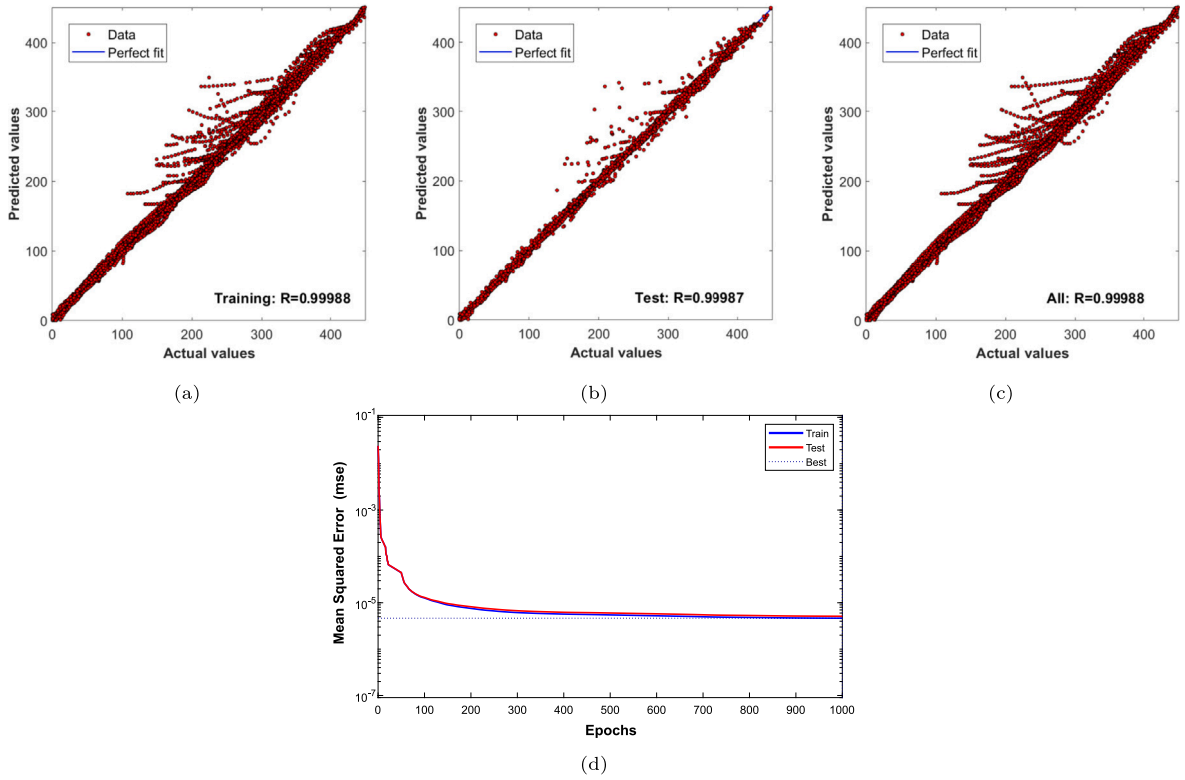

Fig. 15. (a–c) Regression analysis of the multilayer perceptrons (MLPs) network with back-propagation learning algorithms developed to predict rate- and temperature-dependent flow behavior of monolithic Mg and nanocomposites and (d) variation of Mean Square Error (MSE) versus the number of epochs for training and test data sets. Please note that the highest training performance was attained at epoch 1000, with a value of 4.7362e−06.

Fig. 16 demonstrates a comparison between the true stress–strain curves measured experimentally at a variety of strain rates and temperatures and the curves computed using the J–C model. As evident in Fig. 16, the J–C constitutive equation provided a good approximation of the flow stress for the monolithic Mg and the Mg-CeO_2 nanocomposites and was in excellent agreement with the experimental results. Furthermore, Fig. 16 plots the prediction rate- and temperature-dependent deformation response, obtained from the developed MLPs network with back-propagation learning algorithms. From the data plotted in Fig. 16, it is apparent that the network prediction results were in good agreement with the physical experimental data.

A comparison study was conducted between the proposed network and the experimental data obtained from the compression test to further examine the capabilities of the developed MLPs network with back-propagation learning algorithms. Fig. 17 presents a comparison of the YS, UCS, and FS, measured at various strain rates and temperatures during the experimentation and on the basis of the data obtained from the developed network. It appears from Fig. 17 that the yield

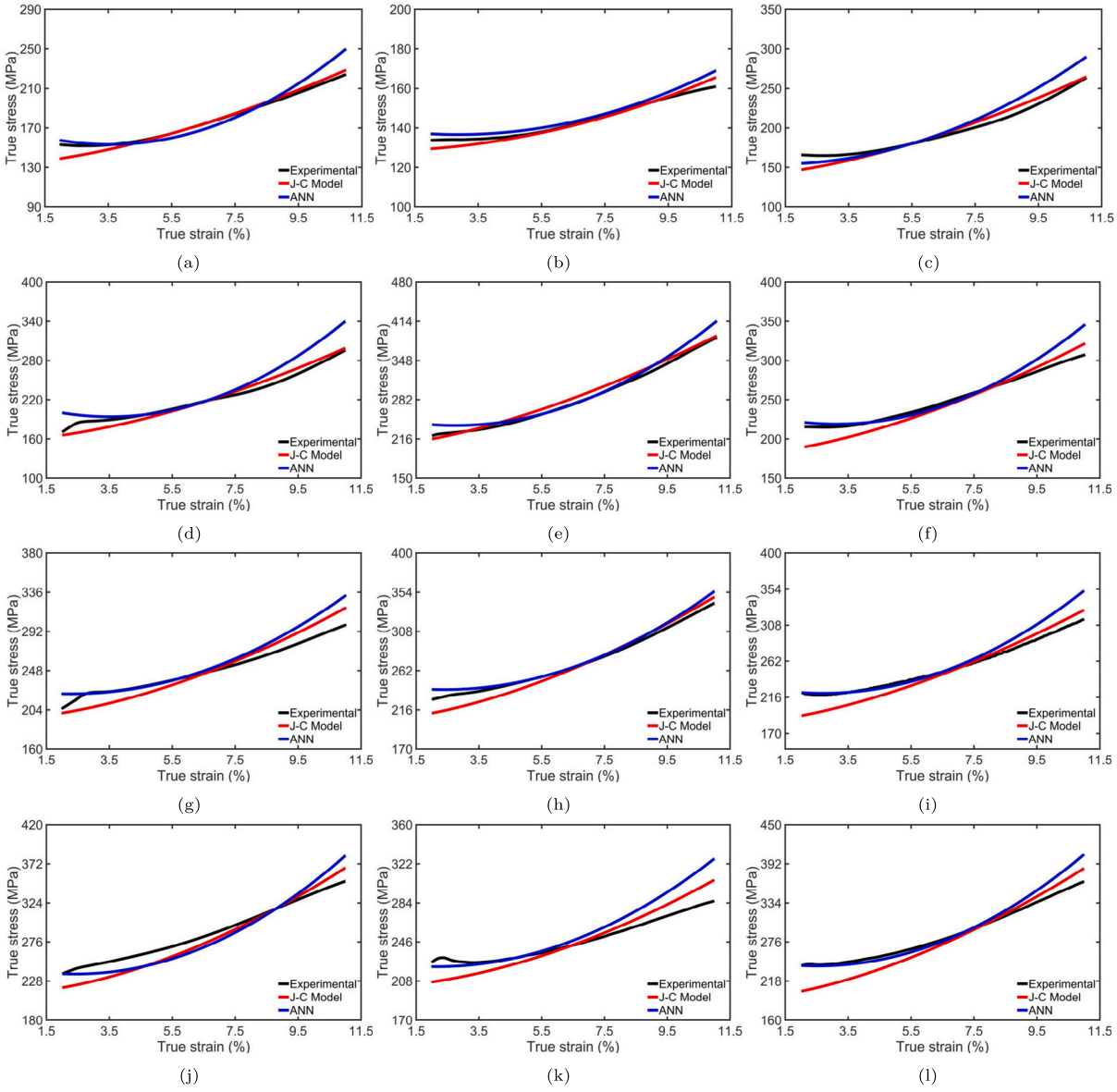

Fig. 16. Comparison between the experimental and the predicted stress–strain curves for (a–c) pure Mg at a strain rate and temperature of 0.001 s^{-1}, 423 K and 0.001 s^{-1}, 473 K, and 0.01 s^{-1}, 423 K respectively; (d–f) Mg-0.5CeO_2 nanocomposites at a strain rate and temperature of 0.001 s^{-1}, 373 K and 0.01 s^{-1}, 373 K, and 0.01 s^{-1}, 423 K respectively; (g–i) Mg-1.0CeO_2 nanocomposites at a strain rate and temperature of 0.0001 s^{-1}, 373 K and 0.001 s^{-1}, 373 K, and 0.01 s^{-1}, 423 K respectively; (j–l) Mg-1.5CeO_2 nanocomposites at a strain rate and temperature of 0.001 s^{-1}, 373 K and 0.001 s^{-1}, 473 K, and 0.01 s^{-1}, 373 K respectively.

and the UCS significantly decreased with the increasing temperature. The increasing temperature, in turn, resulted in an increase in the FS. Here, the developed MLPs network with back-propagation learning algorithms turned out to be reasonably reflecting the strain rate- and temperature-dependent flow behavior of the monolithic Mg and the Mg-CeO_2 nanocomposites. In other words, one could conclude that the MLPs network with back-propagation learning algorithms provided a versatile modeling approach that could be applied to characterize the complex correlations between the multi-inputs and outputs in different contexts.

5. Conclusion

This present study used the mill-press-sinter powder metallurgy techniques in conjunction with hot extrusion to synthesize rare earth reinforced ultrafine Mg-xCeO_2(x = 0.5, 1 and 1.5 vol%) nanocomposites. Investigations on the microstructural and mechanical behavior of nanocomposites were conducted. The main findings are as follows:

1. The proposed Mg-CeO_2 nanocomposites displayed an optimal balance of compressive strength and elongation, which proved to be superior to monolithic Mg and most of the commercially available Mg alloys. Moreover, rare-earth oxides were found to enhance the hardness, the CYS and the UCS of the extruded nanocomposites. A substantial enhancement of 53.84% in hardness was observed in the Mg-1.5CeO_2 nanocomposite as compared to monolithic Mg. The Mg-1.0CeO_2 nanocomposite displayed the highest UCS among all the samples, measuring 559.08 MPa. Additionally, it exhibited a CYS of 294.02 MPa. Under specific strain rate and temperature conditions (0.0001 s^{-1} and 473K, respectively), Mg/1.5CeO_2 exhibits a maximal UCS improvement of 99.06% when compared to pure Mg. Furthermore, the Mg-1.5CeO_2 nanocomposites exhibited a maximal elongation-to-failure of 30.85% at 473 K, which was 28.97% greater than that of pure Mg. The enhanced mechanical properties could be attributed to several factors, such as, the

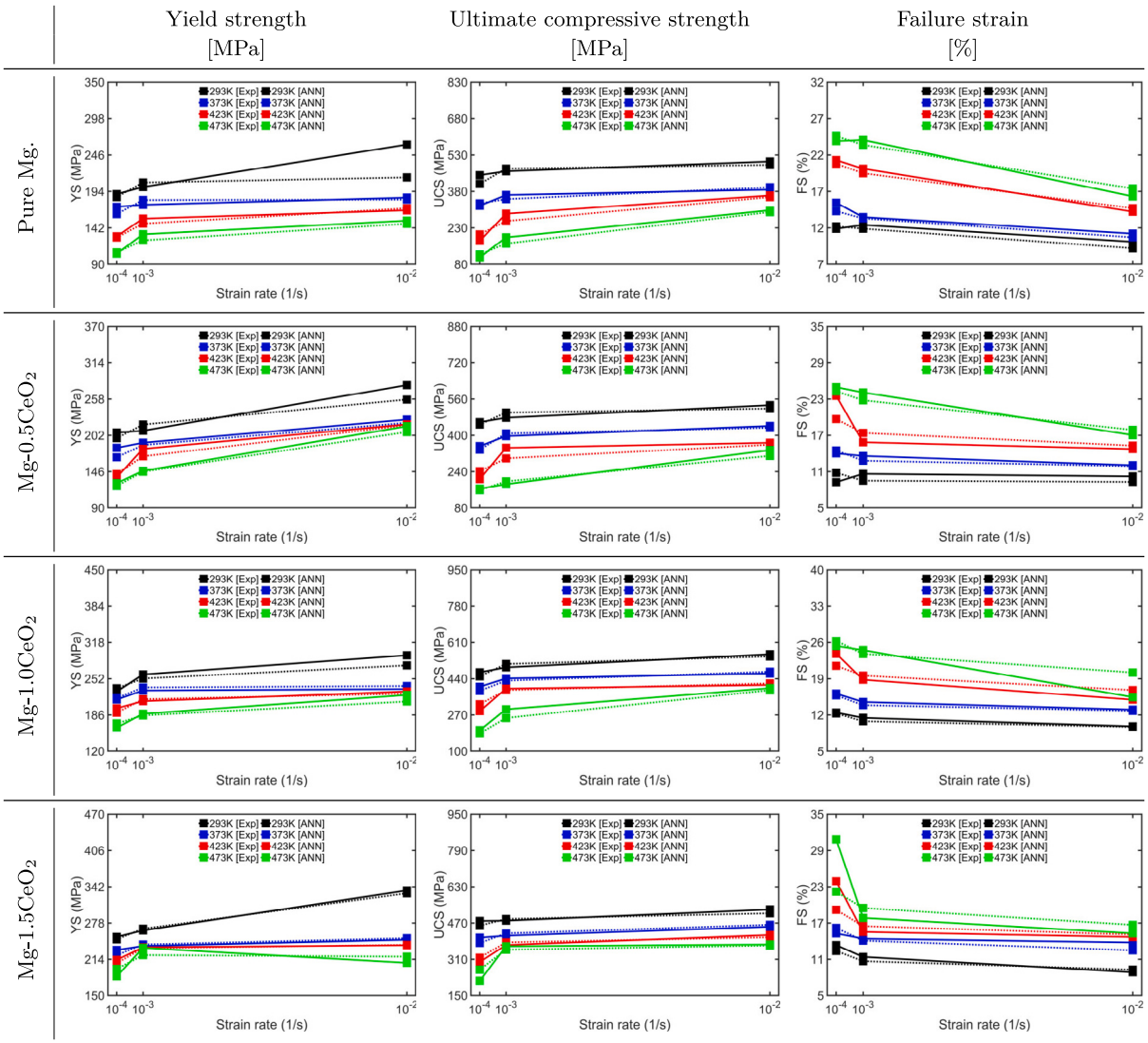

Fig. 17. Comparison between experimental data and the values obtained from the multilayer perceptrons (MLPs) network with back-propagation learning algorithm for YS, UCS, and FS.

microstructure refinement, mismatch of the coefficient of thermal expansion and elastic modulus, Orowan strengthening and dislocation strengthening.

2. The HRTEM analysis of the Mg-CeO_2 nanocomposites indicated the existence of dense dislocations, moiré fringes, and high-angle grain boundaries. Furthermore, the TEM investigation demonstrated the homogeneous dispersion of the CNPs in the Mg matrix.
3. The developed Mg-CeO_2 nanocomposites display substantial temperature and strain rate dependent mechanical characteristics. Mg-0.5CeO_2 exhibited a maximum decline in compressive strength of 64.03% and an increase in elongation of 169.76% when temperature increased from 293 K to 473 K. Furthermore, at 473 K, when the strain rate increased from 0.0001 to 0.01 s^{-1}, Mg-1.0CeO_2 nanocomposites showed a maximum increase in strength of 102.04%, while elongation to failure dropped by 39.01%.

In addition, two different modeling approaches have been introduced to describe strain rate and temperature dependence deformation behavior of monolithic Mg and Mg-CeO_2 nanocomposites. The first approach used the J–C constitutive model with well-calibrated parameters using the experimental data of synthesized samples. The second approach employed the MLPs network with a back-propagation learning algorithm trained on the experimental data set for synthesized samples. Based on a comparative study, it was concluded that these modeling approaches enable an accurate prediction of the deformation behavior of the monolithic Mg and the Mg-CeO_2 nanocomposites at various strain-rates and under different temperatures. As future work, the fatigue behavior of Mg-based nanocomposites can be investigated experimentally and theoretically using a unified microplasticity-based constitutive model [64–66].

CRediT authorship contribution statement

Surja Deka: Methodology, Visualization, Formal analysis, Investigation, Validation, Software, Writing – original draft. **Farzin Mozafari:** Methodology, Investigation, Formal analysis, Software, Writing – original draft. **Ashis Mallick:** Conceptualization, Resources, Supervision.

Declaration of competing interest

The authors declare that they have no known competing financial interests or personal relationships that could have appeared to influence the work reported in this paper.

Table A.1
Summary of the compression properties of monolithic Mg and Mg-xCeO_2(x = 0.5, 1, and 1.5) nanocomposites at different test temperatures and strain rates.

Materials	Strain rate = 0.0001 s^{-1}											
	CYS(MPa)				UCS(MPa)				FS(%)			
	293 K	373 K	423 K	473 K	293 K	373 K	423 K	473 K	293 K	373 K	423 K	473 K
Pure Mg	190±4	171±3	130±2	105±6	448±8	321±9	175±11	107±8	11.88±1.1	15.45±0.3	21.31±0.7	23.92±0.8
Mg-0.5CeO_2	206±2	182±5	137±1	128±9	458±9	352±12	207±9	164±11	9.26±1.9	14.02±0.4	23.54±0.8	24.98±0.2
Mg-1.0CeO_2	228±3	213±4	198±2	163±7	467±9	403±11	289±13	196±8	12.46±0.5	16.13±1.0	23.83±0.2	25.33±0.3
Mg-1.5CeO_2	254±2	230±1	213±6	184±5	477±2	405±3	297±7	213±12	13.36±0.6	15.30±0.6	23.93±0.1	30.85±1.8
	Strain rate = 0.001 s^{-1}											
Pure Mg	199±5	174±6	154±4	132±6	462±10	365±3	289±7	190±6	12.40±0.2	13.48±0.9	20.12±1.1	24.08±0.8
Mg-0.5CeO_2	209±3	190±4	181±1	147±9	477±3	396±2	345±8	184±11	10.63±0.2	13.59±1.2	15.86±0.4	24.10±0.9
Mg-1.0CeO_2	259±4	230±1	210±6	188±3	492±8	441±11	394±4	294±9	11.45±0.4	14.52±1.3	18.81±2.4	24.52±0.3
Mg-1.5CeO_2	264±6	236±1	235±1	234±8	480±2	413±10	373±3	368±7	11.41±0.3	14.42±0.2	15.54±0.5	17.86±1.0
	Strain rate = 0.01 s^{-1}											
Pure Mg	261±7	185±6	167±6	153±4	506±9	390±2	366±8	306±11	10.09±0.6	11.21±0.3	14.22±0.9	16.32±0.8
Mg-0.5CeO_2	279±7	226±5	218±1	216±2	533±8	441±7	367±4	334±10	10.21±0.4	12.05±0.6	14.74±1.2	17.04±0.7
Mg-1.0CeO_2	294±6	232±2	228±3	221±4	559±6	466±9	413±3	396±9	9.81±0.9	13.03±0.4	14.96±0.4	15.45±0.1
Mg-1.5CeO_2	335±6	248±5	238±2	208±7	530±7	455±10	418±3	379±5	8.87±1.1	13.79±0.5	14.70±0.3	15.31±0.9

Data availability

Data will be made available on request.

Acknowledgments

This work was supported by the ASEAN-Indian Science and Technology Development Fund, DST, Govt. of India under Grant no. IMRC/AISTDF/R&D/P-14/2018. F.M. acknowledges the partial support provided by the AGÜ foundation.

Appendix. Compression properties of monolithic Mg and Mg-xCeO_2 nanocomposites

This appendix provides a comprehensive summary of the compression properties of monolithic Mg (pure magnesium) and Mg-xCeO_2 nanocomposites under a wide range of test conditions. The data within this section reports on the mechanical behavior of these materials at varying test temperatures and strain rates, with a particular focus on different x values for cerium oxide (0.5, 1, and 1.5) (see Table A.1).

References

[1] Li X, Shi H, Wang X, Hu X, Xu C, Shao W. Achieving high strength and ductility in GNSs/Mg nanocomposites fabricated by in-situ liquid metallurgy combined with hot extrusion. Composites A 2022;161:107079.
[2] Paramsothy M, Hassan S, Srikanth N, Gupta M. Adding carbon nanotubes and integrating with AA5052 aluminium alloy core to simultaneously enhance stiffness, strength and failure strain of AZ31 magnesium alloy. Composites A 2009;40(9):1490–500.
[3] Qian M, Goh C, Sun Y, Ng F. Effects of CNTs on microstructure and hardness of laser welds of the CNT-reinforced magnesium composite. Composites A 2013;48:67–72.
[4] Ponhan K, Tassenberg K, Weston D, Nicholls KG, Thornton R. Effect of SiC nanoparticle content and milling time on the microstructural characteristics and properties of Mg-SiC nanocomposites synthesized with powder metallurgy incorporating high-energy ball milling. Ceram Int 2020;46(17):26956–69.
[5] Mallick A, Vedantam S, Lu L. Grain size dependent tensile behavior of Mg–3% Al alloy at elevated temperatures. Mater Sci Eng A 2009;515(1–2):14–8.
[6] Kujur MS, Manakari V, Parande G, Prasadh S, Wong R, Mallick A, et al. Development of rare-earth oxide reinforced magnesium nanocomposites for orthopaedic applications: A mechanical/immersion/biocompatibility perspective. J Mech Behav Biomed Mater 2021;114:104162.
[7] Kumar P, Mallick A, Kujur MS, Tun KS, Shabadi R, Gupta M. Strength of Mg–3% Al alloy in presence of graphene nano-platelets as reinforcement. Mater Sci Technol 2018;34(9):1086–95.
[8] Xiang Y, Wang X, Hu X, Meng L, Song Z, Li X, et al. Achieving ultra-high strengthening and toughening efficiency in carbon nanotubes/magnesium composites via constructing micro-nano layered structure. Composites A 2019;119:225–34.
[9] Haghshenas M, Gupta M. Magnesium nanocomposites reinforced with rare earth element nanoparticles: Nanoindentation-driven response. Nanocomposites 2020;6(1):22–30.
[10] Eyring L. The binary rare earth oxides. In: Handbook on the physics and chemistry of rare earths, vol. 3. Elsevier; 1979, p. 337–99.
[11] Kujur MS, Mallick A, Manakari V, Parande G, Tun KS, Gupta M. Significantly enhancing the ignition/compression/damping response of monolithic magnesium by addition of Sm2O3 nanoparticles. Metals 2017;7(9):357.
[12] Kujur MS, Manakari V, Parande G, Tun KS, Mallick A, Gupta M. Enhancement of thermal, mechanical, ignition and damping response of magnesium using nano-ceria particles. Ceram Int 2018;44(13):15035–43.
[13] Zheng Z, Zhao M-C, Tan L, Zhao Y-C, Xie B, Yin D, et al. Corrosion behavior of a self-sealing coating containing CeO2 particles on pure Mg produced by micro-arc oxidation. Surf Coat Technol 2020;386:125456.
[14] Maji P, Nath RK, Paul P, Meitei RB, Ghosh SK. Effect of processing speed on wear and corrosion behavior of novel MoS2 and CeO2 reinforced hybrid aluminum matrix composites fabricated by friction stir processing. J Manuf Process 2021;69:1–11.
[15] Li H, Yuan B, Gao Y, Chung CY, Zhu M. High-porosity NiTi superelastic alloys fabricated by low-pressure sintering using titanium hydride as pore-forming agent. J Mater Sci 2009;44:875–81.
[16] Kandemir S, Gavras S, Dieringa H. High temperature tensile, compression and creep behavior of recycled short carbon fibre reinforced AZ91 magnesium alloy fabricated by a high shearing dispersion technique. J Magn Alloys 2021;9(5):1753–67.
[17] Wang H, Wu P, Kurukuri S, Worswick MJ, Peng Y, Tang D, et al. Strain rate sensitivities of deformation mechanisms in magnesium alloys. Int J Plast 2018;107:207–22.
[18] Zhang C, Lu C, Pei L, Li J, Wang R, Tieu K. The negative Poisson's ratio and strengthening mechanism of nanolayered graphene/Cu composites. Carbon 2019;143:125–37.
[19] Laksmi B, Nouri JM, Brabazon D, Naher S. Prediction of properties for the production and application of graphene reinforced metal matrix composites. Proc SEEP2015 2015.
[20] Bisht A, Srivastava M, Kumar RM, Lahiri I, Lahiri D. Strengthening mechanism in graphene nanoplatelets reinforced aluminum composite fabricated through spark plasma sintering. Mater Sci Eng A 2017;695:20–8.
[21] Zhang F, Liu Z, Wang Y, Mao P, Kuang X, Zhang Z, et al. The modified temperature term on Johnson-Cook constitutive model of AZ31 magnesium alloy with {0002} texture. J Magn Alloys 2020;8(1):172–83.
[22] Liu J, Zhang Y, Zhang Y, Kitipornchai S, Yang J. Machine learning assisted prediction of mechanical properties of graphene/aluminium nanocomposite based on molecular dynamics simulation. Mater Des 2022;213:110334.
[23] Najjar I, Sadoun A, Alsoruji GS, Abd Elaziz M, Wagih A. Predicting the mechanical properties of Cu–Al2O3 nanocomposites using machine learning and finite element simulation of indentation experiments. Ceram Int 2022;48(6):7748–58.
[24] Guo S, Zhang X, Shi C, Zhao D, He C, Zhao N. Continuous confined interfacial design in graphene/Cu composites with structural integrity enables improvement of comprehensive properties. Composites A 2023;169:107525.

[25] Rahmani K, Nouri A, Wheatley G, Malekmohammadi H, Bakhtiari H, Yazdi V. Determination of tensile behavior of hot-pressed Mg–TiO2 and Mg–ZrO2 nanocomposites using indentation test and a holistic inverse modeling technique. J Mater Res Technol 2021;14:2107–14.
[26] Razavi M, Fathi M, Meratian M. Microstructure, mechanical properties and biocorrosion evaluation of biodegradable AZ91-FA nanocomposites for biomedical applications. Mater Sci Eng: A 2010;527(26):6938–44.
[27] Rahmani K, Majzoobi G, Sadooghi A, Kashfi M. Mechanical and physical characterization of Mg-TiO2 and Mg-ZrO2 nanocomposites produced by hot-pressing. Mater Chem Phys 2020;246:122844.
[28] Saheb N. Characterization of mechanically milled and spark plasma sintered Al2124-CNT nanocomposites. Sci Sintering 2015;47(2).
[29] Benjamin JS. Dispersion strengthened superalloys by mechanical alloying. Metall Trans 1970;1(10):2943–51.
[30] Fogagnolo J, Velasco F, Robert M, Torralba J. Effect of mechanical alloying on the morphology, microstructure and properties of aluminium matrix composite powders. Mater Sci Eng A 2003;342(1–2):131–43.
[31] Ma H, Wang J, Wang H, Dong N, Zhang J, Jin P, et al. Influence of nano-diamond content on the microstructure, mechanical and thermal properties of the ZK60 composites. J Magnes Alloys 2022;10(2):440–8.
[32] Ferguson J, Sheykh-Jaberi F, Kim C-S, Rohatgi PK, Cho K. On the strength and strain to failure in particle-reinforced magnesium metal-matrix nanocomposites (Mg MMNCs). Mater Sci Eng A 2012;558:193–204.
[33] Fu X, Deng R, Kong X, Parande G, Hu J, Peng P, et al. Interfacial characterization and its influence on the corrosion behavior of Mg-SiO2 nanocomposites. Acta Mater 2022;230:117840.
[34] Manu KS, Kumar SA, Rajan T, Mohammed MR, Pai B. Effect of alumina nanoparticle on strengthening of Al-Si alloy through dendrite refinement, interfacial bonding and dislocation bowing. J Alloys Compd 2017;712:394–405.
[35] Paramsothy M, Chan J, Kwok R, Gupta M. Enhanced mechanical response of magnesium alloy ZK60A containing Si3N4 nanoparticles. Composites A 2011;42(12):2093–100.
[36] Mirza F, Daolun C, Dejiang L, Xiaoqin Z. A modified Johnson-Cook constitutive relationship for a rare-earth containing magnesium alloy. J Rare Earths 2013;31(12):1202–7.
[37] Li J, Xu W, Wu X, Ding H, Xia K. Effects of grain size on compressive behaviour in ultrafine grained pure Mg processed by equal channel angular pressing at room temperature. Mater Sci Eng A 2011;528(18):5993–8.
[38] Khodabakhshi F, Gerlich A, Simchi A, Kokabi A. Hot deformation behavior of an aluminum-matrix hybrid nanocomposite fabricated by friction stir processing. Mater Sci Eng A 2015;626:458–66.
[39] Mallick A, Tun KS, Gupta M. Deformation behaviour of Mg/Y2o3 nanocomposite at elevated temperatures. Mater Sci Eng A 2012;551:222–30.
[40] Subramani M, Huang S-J, Borodianskiy K. Effect of SiC nanoparticles on AZ31 magnesium alloy. Materials 2022;15(3):1004.
[41] Paramsothy M, Chan J, Kwok R, Gupta M. Addition of CNTs to enhance tensile/compressive response of magnesium alloy ZK60A. Compos A: Appl Sci Manuf 2011;42(2):180–8.
[42] Sankaranarayanan S, Sabat R, Jayalakshmi S, Suwas S, Almajid A, Gupta M. Mg/BN nanocomposites: nano-BN addition for enhanced room temperature tensile and compressive response. J Compos Mater 2015;49(24):3045–55.
[43] Sankaranarayanan S, Habibi M, Jayalakshmi S, Jia Ai K, Almajid A, Gupta M. Nano-AlN particle reinforced Mg composites: Microstructural and mechanical properties. Mater Sci Technol 2015;31(9):1122–31.
[44] Habibi MK, Hamouda AS, Gupta M. Hybridizing boron carbide (B4C) particles with aluminum (Al) to enhance the mechanical response of magnesium based nano-composites. J Alloys Compd 2013;550:83–93.
[45] Hassan S, Gupta M. Effect of particulate size of al2o3 reinforcement on microstructure and mechanical behavior of solidification processed elemental Mg. J Alloys Compd 2006;419(1–2):84–90.
[46] Wong WE, Gupta M. Effect of hybrid length scales (micro+ nano) of SiC reinforcement on the properties of magnesium. Solid State Phenomena 2006;111:91–4.
[47] Meenashisundaram GK, Nai MH, Almajid A, Gupta M. Development of high performance Mg–TiO2 nanocomposites targeting for biomedical/structural applications. Mater Des (1980-2015) 2015;65:104–14.
[48] Rahmani K, Sadooghi A, Nokhberoosta M. The effect of the double-action pressure on the physical, mechanical and tribology properties of Mg-WO3 nanocomposites. J Mater Res Technol 2020;9(1):1104–18.
[49] Ding Y, Xu J, Hu J, Gao Q, Guo X, Zhang R, et al. High performance carbon nanotube-reinforced magnesium nanocomposite. Mater Sci Eng A 2020;771:138575.
[50] Suryanarayana C. Mechanical alloying and milling. Prog Mater Sci 2001;46(1–2):1–184.
[51] Zhu Y, Qin J, Wang J, Jin P, Li P. Significant strain hardening ability of AZ91 magnesium alloy fabricated by spark plasma sintering. Mater Today Commun 2023;35:105670.
[52] Peng P, Zhang L, Zhao J, Ran C, Wang B, Long S, et al. Simultaneous improvement of strength and ductility in ZK60 magnesium alloy by constructing the bimodal grain structure. J Mater Res Technol 2023;22:1026–38.
[53] Song B, Xin R, Chen G, Zhang X, Liu Q. Improving tensile and compressive properties of magnesium alloy plates by pre-cold rolling. Scr Mater 2012;66(12):1061–4.
[54] Chen Y, Guo Y, Gupta M, Shim V. A study of the dynamic compressive response of AZ31/Al2O3 nanocomposites and the influence of nanoparticles. Int J Impact Eng 2016;89:114–23.
[55] Fan L, Zhou M, Zhang Y, Dieringa H, Qian X, Zeng Y, et al. Achieving high strength and ductility in a heterogeneous bimodal grain structured TiC/AZ61 magnesium nanocomposites via powder metallurgy. Mater Sci Eng A 2023;867:144344.
[56] Kim C-S, Sohn I, Nezafati M, Ferguson J, Schultz BF, Bajestani-Gohari Z, et al. Prediction models for the yield strength of particle-reinforced unimodal pure magnesium (Mg) metal matrix nanocomposites (MMNCs). J Mater Sci 2013;48:4191–204.
[57] Wang J, Yuan X, Jin P, Ma H, Shi B, Zheng H, et al. Study on modified johnson-cook constitutive material model to predict the dynamic behavior Mg-1Al-4Y alloy. Mater Res Exp 2020;7(2):026522.
[58] Çolak AB. An experimental study on the comparative analysis of the effect of the number of data on the error rates of artificial neural networks. Int J Energy Res 2021;45(1):478–500.
[59] Mao G, Wang M, Liu J, Wang Z, Wang K, Meng Y, et al. Comprehensive comparison of artificial neural networks and long short-term memory networks for rainfall-runoff simulation. Phys Chem Earth A/B/C 2021;123:103026.
[60] Kapoor R, Pal D, Chakravartty J. Use of artificial neural networks to predict the deformation behavior of Zr–2.5 Nb–0.5 Cu. J Mater Process Technol 2005;169(2):199–205.
[61] Mandal S, Sivaprasad P, Venugopal S, Murthy K. Constitutive flow behaviour of austenitic stainless steels under hot deformation: Artificial neural network modelling to understand, evaluate and predict. Modelling Simul Mater Sci Eng 2006;14(6):1053.
[62] MacKay DJ. A practical Bayesian framework for backpropagation networks. Neural Comput 1992;4(3):448–72.
[63] Burden F, Winkler D. Bayesian regularization of neural networks. In: Artificial neural networks: methods and applications. Springer; 2009, p. 23–42.
[64] Mozafari F, Thamburaja P, Moslemi N, Srinivasa A. Finite-element simulation of multi-axial fatigue loading in metals based on a novel experimentally-validated microplastic hysteresis-tracking method. Finite Elem Anal Des 2021;187:103481.
[65] Mozafari F, Temizer I. Computational homogenization of fatigue in additively manufactured microlattice structures. Comput Mech 2022;1–18.
[66] Mozafari F, Thamburaja P, Srinivasa A, Moslemi N. A rate independent inelasticity model with smooth transition for unifying low-cycle to high-cycle fatigue life prediction. Int J Mech Sci 2019;159:325–35.